Draft version January 1, 2022
Typeset using LaTeX **twocolumn** style in AASTeX63

arXiv:2008.02806v1 [astro-ph.GA] 6 Aug 2020

Hyper Suprime-Cam Low Surface Brightness Galaxies II: A Hubble Space Telescope Study of the Globular Cluster Systems of Ultra-Diffuse Galaxies in Groups*

Jean J. Somalwar,[1] Jenny E. Greene,[1] Johnny P. Greco,[2,†] Song Huang,[1] Rachael L. Beaton,[1] Andy D. Goulding,[1] and Lachlan Lancaster[1]

[1] *Department of Astrophysical Sciences, 4 Ivy Lane, Princeton University, Princeton, NJ 08544, USA*
[2] *Center for Cosmology and AstroParticle Physics (CCAPP), The Ohio State University, Columbus, OH 43210, USA*

(Received; Revised; Accepted)

Submitted to ApJ

ABSTRACT

We increase the sample of ultra diffuse galaxies (UDGs) in lower density environments with characterized globular cluster (GC) populations using new *Hubble Space Telescope* observations of nine UDGs in group environments. While the bulk of our UDGs have GC abundances consistent with normal dwarf galaxies, two of these UDGs have excess GC populations. These two UDGs both have GC luminosity functions consistent with higher surface brightness galaxies and cluster UDGs. We then combine our nine objects with previous studies to create a catalog of UDGs with analyzed GC populations that spans a uniquely diverse range of environments. We use this catalog to examine broader trends in the GC populations of low stellar mass galaxies. The highest GC abundances are found in cluster UDGs, but whether cluster UDGs are actually more extreme requires study of many more UDGs in groups. We find a possible positive correlation between GC abundance and stellar mass, and between GC abundance and galaxy size at fixed stellar mass. However, we see no significant stellar-mass galaxy-size relation, over our limited stellar mass range. We consider possible origins of the correlation between GC abundance and galaxy size, including the possibility that these two galaxy properties are both dependent on the galaxy dark matter halo, or that they are related through baryonic processes like internal feedback.

1. INTRODUCTION

Low surface brightness galaxies (LSBGs) are a powerful probe of the coupling between baryons and the dark matter halos they inhabit. Ultra-diffuse galaxies (UDGs), which are characterized by central surface brightnesses $\mu_{0,g} > 24$ mag arcsec^{-2} and sizes $r_{\rm eff} > 1.5$ kpc, are especially sensitive to the astrophysics of star formation and feedback. UDGs have been known to exist since the 1980s (e.g. Sandage & Binggeli 1984; Impey et al. 1988; Dalcanton et al. 1997; Conselice et al. 2003), but it has only recently become possible to build large samples of such low surface brightness objects across galaxy environments using deep, wide-field imaging surveys. The discovery of a large population of UDGs in the Coma Cluster by the low-surface-brightness-optimized Dragonfly Array (Abraham & van Dokkum 2014; van Dokkum et al. 2015) has reignited the search for such objects, leading to the discovery of thousands of UDGs in Coma and other clusters (Koda et al. 2015; Yagi et al. 2016; Van Der Burg et al. 2016; Lee et al. 2020; Piña et al. 2019), as well as in lower density environments (e.g. Leisman et al. 2017; Greco et al. 2018b; Román & Trujillo 2017; Van Der Burg et al. 2017).

Despite this monumental increase in sample size, many puzzles surround UDGs; in particular, their formation mechanism is unclear. We can separate the proposed UDG formation models by their predicted halo masses. At the typical UDG stellar mass ($\sim 10^8\,M_\odot$), we expect halo masses $M_{\rm halo} \sim 10^{10-11}\,M_\odot$. If UDGs occupy this $M_{\rm halo}$ range, they may be outliers in their surface brightness due to high angular momentum halos, strong stellar outflows, or tidal stripping (e.g. Amorisco & Loeb 2016; Carleton et al. 2019; Liao et al. 2019; Di Cintio et al. 2017; Jiang et al. 2019; El-Badry et al. 2016). On the other hand, if UDGs have large halo masses $M_{\rm halo} \sim 10^{11-12}\,M_\odot$, they may be produced by, e.g., the "failed-L_*" mechanism, which forms UDGs as

Corresponding author: Jean J. Somalwar
jsomalwar@gmail.com

* Based on observations made with the NASA/ESA Hubble Space Telescope, obtained at the Space Telescope Science Institute, which is operated by the Association of Universities for Research in Astronomy, Inc., under NASA contract NAS 5-26555. These observations are associated with programs GO-15277

† NSF Astronomy & Astrophysics Postdoctoral Fellow

normal L_* galaxies which suffer early quenching (van Dokkum et al. 2015; Yozin & Bekki 2015).

This large variation in possible halo masses for UDGs reflects the complex nature of the galaxy-halo connection in the dwarf regime, which we can quantify with the stellar-to-halo mass relation (SHMR) (Wechsler & Tinker 2018). The SHMR is a correlation between M_* and $M_{\rm halo}$. It is often modelled as a broken power law with a break near $M_* \sim 10^{12}\,M_\odot$ and lognormal scatter. At low M_* ($\lesssim 10^{8-9}\,M_\odot$), observations are limited and the slope and scatter of the SHMR become very degenerate, so the level of scatter is heavily debated (e.g. Garrison-Kimmel et al. 2016; Cao et al. 2019).

Therefore, it is important to constrain the halo masses of UDGs to better understand their formation, and more broadly how they affect the SHMR at low stellar masses. There are two main avenues to better understanding UDG halo masses. First, cosmological simulations contain UDG-like galaxies that are roughly consistent with the standard SHMR, but not objects in overly massive halos (Carleton et al. 2019; Liang et al. 2016; Jiang et al. 2019; Di Cintio et al. 2017). Those simulations which contain $M_{\rm halo} \lesssim 10^{11}\,M_\odot$ UDGs disagree about the precise mechanism driving the large galaxy effective radii. For example, simulations disagree about the importance of halo spin in forming UDGs (Carleton et al. 2019; Liao et al. 2019; Di Cintio et al. 2017; Tremmel et al. 2019).

Second, UDG halo masses can be constrained observationally using measurements of weak lensing (Sifón et al. 2018), dynamics (Beasley et al. 2016; van Dokkum et al. 2017, 2018a,b; Danieli et al. 2019), and X-ray emission (Kovács et al. 2019; Kovacs et al. 2020). Such work has suggested that UDGs have halo masses covering the entire range from $M_{\rm halo} \sim 10^8\,M_\odot$ to $M_{\rm halo} \sim 10^{12}\,M_\odot$, or from dwarf masses to L_* or larger. (e.g. van Dokkum et al. 2017, 2018a,b; Danieli et al. 2019). However, due to the technical challenges involved with observing low surface brightness objects, these methods of constraining halo masses have only yielded individual halo masses for a small number of targets.

Alternatively, one can potentially measure halo masses with globular cluster (GC) abundance, which we will refer to as $N_{\rm GC}$. A correlation between $N_{\rm GC}$ and $M_{\rm halo}$ is suggested by the U-shaped distribution of $N_{\rm GC}$ as a function of galaxy stellar mass (e.g. Harris & van den Bergh 1981; Peng et al. 2008; Blakeslee et al. 1997). Such a correlation has been observed in high surface brightness galaxies (Harris et al. 2013, 2017), and comparisons of dynamical UDG masses to GC counts have suggested that the same correlation is valid in the UDG regime (Beasley et al. 2016; Toloba et al. 2018). GCs are gravitationally bound clumps of stars which form early and have typical masses $M_* \sim 10^5\,M_\odot$ and mass-to-light ratios $(M_*/L_V)/(M_*/L_V)_\odot \sim 2$ (Ebrahimi et al. 2020). They have a typical size ∼10 pc, corresponding to $\sim 0\farcs02$ at a distance ∼100 Mpc (Kruijssen 2014). The theoretical basis for the connection between GC abundance and dark matter halo mass is hotly debated. Simulations can reproduce the correlation by invoking tidal disruption in the dense disks where GCs form (e.g. Kruijssen 2015), but it has also been reproduced at $M_{\rm halo} \gtrsim 10^{11.5}\,M_\odot$ using hierarchical merging, with no dependence on the GC formation history (El-Badry et al. 2019).

Although some UDGs have small GC populations consistent with dwarf galaxies (e.g. Amorisco et al. 2016; Forbes et al. 2018), a number of UDGs have very rich GC populations (e.g. Peng & Lim 2016; van Dokkum et al. 2017), which could suggest that the UDGs are produced by a mechanism which also predicts high halo masses. However, the objects with large GC populations are all located in clusters, raising the question of whether GC-rich UDGs are unique to high density environments. The LSBG catalog from Greco et al. (2018b) provides a unique opportunity to explore this possibility with its large environment- and color-blind sample of LSBGs. Thus, in this paper we will use *Hubble Space Telescope* (*HST*) observations of nine Greco et al. (2018b) UDGs in group environments to constrain the GC populations of UDGs in lower density environments (Greco et al. 2017).

In Section 2, we describe our observations and data reduction procedure. In Section 3, we describe our procedure to identify GCs associated with our UDGs. In Section 4, we describe the GC populations of our UDGs. Then, we place our work in a broader context by comparing our observations with literature results in Section 5. We will analyze the relationship between GC abundance, galaxy stellar mass, and galaxy size in Section 6. Finally, we will summarize and conclude in Section 7.

We adopt a standard flat ΛCDM model with $\rm H_0 = 70$ km s^{-1} Mpc^{-1} and $\Omega_{\rm m} = 0.3$. All magnitudes are reported in the AB system.

2. DATA

2.1. *Sample Selection*

We selected a sample of UDGs in two groups from the Greco et al. (2018b) catalog. Greco et al. (2018b) designed a custom search of Hyper Suprime-Cam (HSC) data and identified ∼800 LSBGs over ∼200 deg^2 (Bosch et al. 2018; Aihara et al. 2018). Within this parent sample, we selected UDGs projected near two galaxy groups of known distance. These groups were identified in the SDSS galaxy groups survey using a friends-of-friends halo finder, and were assigned halo masses based on total r-band luminosity (Yang et al. 2007). Of the UDGs in these groups, we selected the proposed sample to be as large as possible while still spanning the full range of galaxy color available. The groups and the selected UDGs are shown in Figure 1. Group A, con-

Table 1. Summary of ultra-diffuse galaxy properties

Galaxy	RA [J2000]	Decl. [J2000]	m_V [mag]	$\mu_0(g)$ [mag arcsec^{-2}]	m_g [mag]	$r_{\rm eff}$ [arcsec]	$r_{\rm eff}$ [kpc]	log $M_*/M_\odot$
UDG-1A	09:18:45.32	+00:24:01.40	19.5 ± 0.4	24.1 ± 0.2	19.9 ± 0.2	6.2 ± 0.8	2.1 ± 0.3	7.9 ± 0.3
UDG-3A	09:19:55.56	+01:07:23.77	20.0 ± 0.4	24.2 ± 0.2	20.3 ± 0.2	4.6 ± 0.8	1.6 ± 0.3	7.7 ± 0.3
UDG-4A	09:18:55.41	+01:45:05.69	19.7 ± 0.4	24.9 ± 0.2	20.0 ± 0.2	9.5 ± 0.8	3.3 ± 0.3	7.8 ± 0.3
UDG-5A	09:19:59.20	+00:48:52.63	20.1 ± 0.4	25.6 ± 0.2	20.2 ± 0.2	8.2 ± 0.8	2.9 ± 0.3	7.6 ± 0.3
UDG-1B	12:04:46.26	+01:17:54.20	19.6 ± 0.4	23.8 ± 0.2	19.6 ± 0.2	5.2 ± 0.8	2.2 ± 0.3	8.0 ± 0.3
UDG-2B	12:04:07.86	+01:19:17.62	20.1 ± 0.4	24.1 ± 0.2	20.0 ± 0.2	5.5 ± 0.8	2.3 ± 0.3	7.8 ± 0.3
UDG-3B	12:04:33.60	+01:24:57.31	20.1 ± 0.4	24.2 ± 0.2	20.0 ± 0.2	4.7 ± 0.8	2.0 ± 0.3	7.8 ± 0.3
UDG-4B	12:02:37.06	+01:30:27.00	20.0 ± 0.4	24.7 ± 0.2	19.9 ± 0.2	7.6 ± 0.8	3.2 ± 0.3	7.8 ± 0.3
UDG-5B	12:06:30.00	+01:33:22.75	21.4 ± 0.4	26.0 ± 0.2	21.1 ± 0.2	5.4 ± 0.8	2.2 ± 0.3	7.3 ± 0.3

NOTE—Galaxy properties determined from the Greco et al. (2018b) catalog. We assume a distance of ∼75 (90) Mpc for UDGs in group A (B) (Yang et al. 2007). The V-band magnitude, M_V, is calculated as $M_V = M_g - 0.59(M_g - M_r) - 0.01$ (Jester et al. 2005). The stellar masses are calculated assuming a solar mass-to-light ratio. We assume that the stellar mass error is 0.3 dex.

taining UDGs 1A, 3A, 4A, and 5A[1], has a host halo mass $10^{12.5}\,M_\odot$ and $z = 0.017$ (∼75 Mpc) (Yang et al. 2007). UDGs 1-5B are located in group B with a host halo mass $10^{13.9}\,M_\odot$ and $z = 0.0206$ (∼90 Mpc). These UDGs have g-band central surface brightnesses ranging from $23.8 - 26$ mag arcsec^{-2} and effective radii from $2.5 - 3.5$ kpc (Greco et al. 2018b). Properties of the UDGs, calculated assuming the group distances, are detailed in Table 1. Stellar-mass-to-light ratios for UDGs and dwarfs are typically of order unity (e.g. Greco et al. 2018a; Pandya et al. 2018), so we calculate the stellar masses assuming $(M_*/L_V)/(M_*/L_V)_\odot = 1$. This assumption is an oversimplification, but we do not currently have the data needed to better constrain M_*/L_V. We discuss possible problems with this assumption in Section 7. We use the galaxy sizes presented in Greco et al. (2018b), which are measured with a single Sérsic fit. We calculate the UDG V-band magnitudes using the HSC photometry and the conversions in Jester et al. (2005).

2.2. *Hubble Space Telescope Data*

We obtained deep follow up of the UDGs with the Wide Field Channel (WFC) of the Advanced Camera for Surveys (ACS) on the *Hubble Space Telescope* (*HST*) (PID 15277, PI J. Greco; Greco et al. (2017)). ACS has the small angular resolution (∼0.″1) necessary to reliably differentiate between point sources (e.g., GCs) and background galaxies. We observed each UDG with the F814W filter (one orbit split into two 2486 sec dithers) and the F606W filter (one orbit split into two 2624 sec dithers). We chose these filters because we can achieve comparable depth in each with a single orbit.

We calibrated the data using the default `calacs` pipeline. The images had significant cosmic ray (CR) contamination, so we used `LACosmicX`[2] (van Dokkum 2001) to perform an initial CR removal. `LACosmicX` uses Laplacian edge detection to identify CR contaminated pixels. We required a Laplacian-to-noise of 6σ to identify a contaminated pixel, a fractional detection limit of 0.5 for flagging pixels bordering an identified CR, and we defined the contrast limit between a CR and an underlying object with a Laplacian-to-noise of 6σ. We then used `DrizzlePac` to remove the remaining CRs. `DrizzlePac` flags CR contaminated pixels as those which are only bright in one dither. We required a CR threshold of 15σ and a convolution kernel width of 3.5 pix.

3. GLOBULAR CLUSTER CANDIDATE DETECTION

In this section, we describe our GC detection procedure. First, we will summarize our overall detection approach, and then we will describe and motivate the detailed choices that we made.

3.1. *Source Identification*

To maximize our sensitivity to GCs, we identify point sources in each galaxy using the sum of the F814W and F606W images. We use these source positions to perform aperture photometry on the individual F814W and F606W images. We subtract the background from the high signal-to-noise detection image using a masked, sigma-clipped median subtraction. We perform this subtraction using a series of steps. First, we use `Photutils`

[1] The UDG 2A observation was unsuccessful because the guide star acquisition failed.

[2] https://github.com/cmccully/lacosmicx

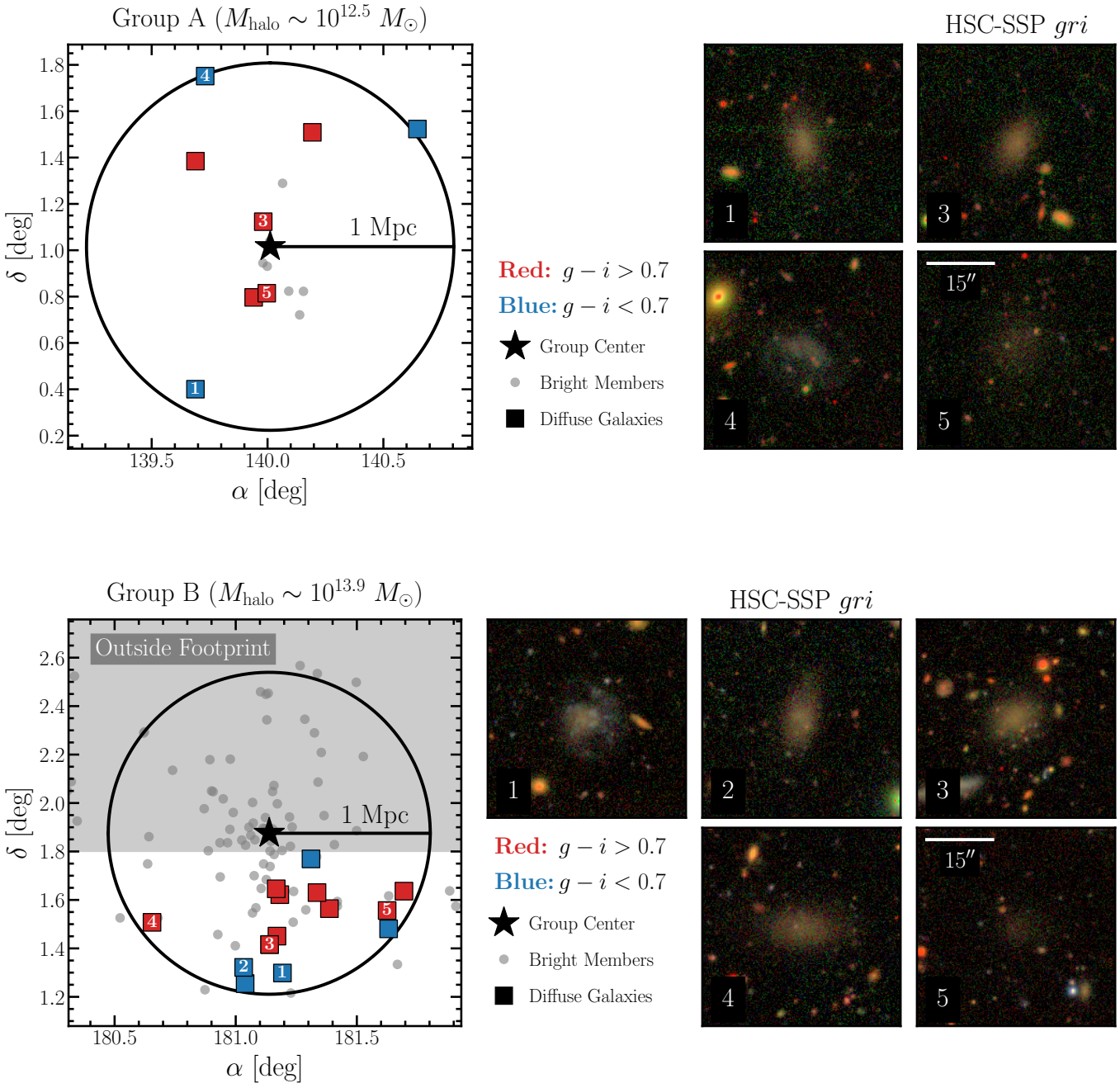


Figure 1. Summary of the UDG sample selection. The UDGs are contained in galaxy groups A ($z = 0.017$, host halo mass $M_{\rm host} = 10^{12.5}\ M_\odot$) and B ($z = 0.0206$, $M_{\rm host} = 10^{13.9}\ M_\odot$). The *left* panels show the placement of galaxies within group A (*top*) and group B (*bottom*). UDGs are shown as squares with color indicating the galaxy color, and galaxies from the SDSS catalogues are shown as gray dots. The UDGs analyzed in this work are numbered. The *right* panels show color Hyper Suprime-Cam images of the nine UDGs analyzed in this work.

to create a source mask of the image (Bradley et al. 2019). We require that the sources included in this mask contain at least 3 pixels above a signal-to-noise threshold of 10. We mask a region around each source which extends to twice the source size. Next, we create the background map for the masked image by running a sigma-clipped median smoothing with box size of 10×10 pix^2.

We detect point sources on the background subtracted detection image using `Photutils`. We require that sources have at least 3 pixels above a detection threshold of 5σ. We then measure source fluxes on the individual F814W and F606W images and account for background by correcting each source flux by the background level in a circular annulus of inner (outer) radius 6 (10) pix. We measure magnitudes in apertures of radius 2, 3.5, and 4 pixels with an initial magnitude zeropoint of 26.0 mag. We correct the magnitudes for aperture effects using the mock GC tests in Section 3.2.

Many of the recovered sources are background galaxies, residual CRs, and intra-group GCs. We first apply a cut on the source concentration, defined as $c = c_2 - c_{3.5}$, where c_i is the magnitude measured in the F606W band using an i-pixel radius aperture (e.g. Peng et al. 2011). This cut removes both very extended and very localized objects, namely, extended background galaxies and CRs that contaminate a small number of pixels. Background galaxies at higher redshift can appear as point sources and cannot be removed with a concentration cut, but they have distinctive red optical colors and can be safely removed by applying a cut on $m_{V_{F606W}} - m_{\rm I_{F814W}}$. We optimize these cuts using mock GC detection tests, described in Section 3.2. After this step, $\sim$20% of the original point sources within $2r_{\rm eff}$ of each UDG remain, and these remaining sources are shown in blue in Figure 2 for UDGs 3A, 5A, 3B, and 4B.

After these cuts, point sources that are intra-group GCs, compact background galaxies, or even background fluctuations will remain. We will call these 'background'. We subtract out this background contribution statistically using a measure of the average background level over the full field. First, we define GCs associated with the UDG as those in an elliptical aperture with semi-major axis $2r_{\rm eff}$ centered on the UDG (e.g. Beasley & Trujillo 2016), as shown in green in Figure 2. We choose a region size of $2r_{\rm eff}$ because we expect it to contain most of the GC population, but it is not so large that background contamination will be prohibitive. We find that variations on region size larger and smaller than $2r_{\rm eff}$ do not significantly change our results. To estimate the background in this 'galaxy region', we randomly fill each *HST* image with apertures of the same size and shape as the galaxy region. We require that these 'background regions' do not overlap with the galaxy region or with one another. We find the average number of sources in each background region that pass our concentration and color cuts, and define this as our background source density. In this average, we do not include those background regions that overlap with 'bad' areas of the image, such as chip gaps or saturated stars. Before applying any completeness correction, we find $\sim$0.3 background sources/arcsec, corresponding to $\sim$3 background sources within $2r_{\rm eff}$ of the typical UDG.

3.2. *Mock Globular Cluster Tests*

To optimize the aforementioned color and concentration cuts and to assess our completeness, we injected mock GCs in 30 random locations in a circular region of radius $5r_{\rm eff}$ around each UDG. We drew the GC magnitudes from the typical observed GC luminosity function (GCLF) modeled as a Gaussian with mean $M_V = -7.3$ mag and $\sigma = 1.1$ mag (Miller & Lotz 2007). We converted the V-band magnitude to F606W assuming $m_V - m_{V_{F606W}} = 0.13$ mag. We drew the GC $m_V - m_{\rm I}$ from a uniform distribution over the range of expected GC colors $[0.3, 1.3]$ mags. Since $m_{\rm I} = m_{\rm I_{F814W}} + \sim$0.01 mag, this color range corresponds to $m_{V_{F606W}} - m_{\rm I_{F814W}} \in [0.17, 1.17]$ mags. We created the mock GCs using `TinyTim` PSFs (Krist et al. 2011), normalized and scaled by $10^{-0.4\times(m-ZP)}$, where m is the mock GC magnitude. We retrieved the zeropoints ZP(F606W) and ZP(F814W) from the *HST* ACS website for the observation dates 2019-03-20, 2019-07-02, 2019-07-03, 2019-05-14, 2019-03-24, 2019-05-16, and 2019-07-04. The zeropoints were ZP(F606W) = 26.50 mag, and ZP(F814W) = 25.94 mag for all of the observations. We created 50 GC-enriched images by repeating this injection process.

We ran `Photutils` to detect GC candidates in each GC-enriched image following the same procedure as for our fiducial analysis. We recovered $\sim$75% of the injected sources. We used the recovered mock GC magnitudes to correct the 4-pixel aperture magnitude zeropoint for, e.g., aperture effects. We subtracted the recovered magnitude from the true magnitude, shown for UDG 5A as a function of true $m_{V_{F606W}}$ in Figure 3. The magnitude zeropoint correction is the average of this magnitude difference for the brightest recovered sources ($m_{V_{F606W}} \lesssim 26$). We found that all UDGs required ZP(F606W) = 26.34 mag, and ZP(F814W) = 25.79 mag. We use the scatter in the zeropoint correction to estimate a magnitude error of $\pm$0.15. We also use the scatter in the recovered color to estimate a color error of $\pm$0.2.

We then optimized our color and concentration cuts. In Figure 4, we show histograms of the recovered mock GC color and $c_{2-3.5}$ for UDG 5A. We define our cut on each variable as the interval which contains 95% of the injected GCs, shown as vertical lines in Figure 4. Since we apply a statistical background cut as described in Section 3.1, we aim to maximize completeness over purity with these cuts. We list these cuts for each galaxy in Table 2. We also show the resulting completeness curves for each galaxy in Figure 5. Given these com-

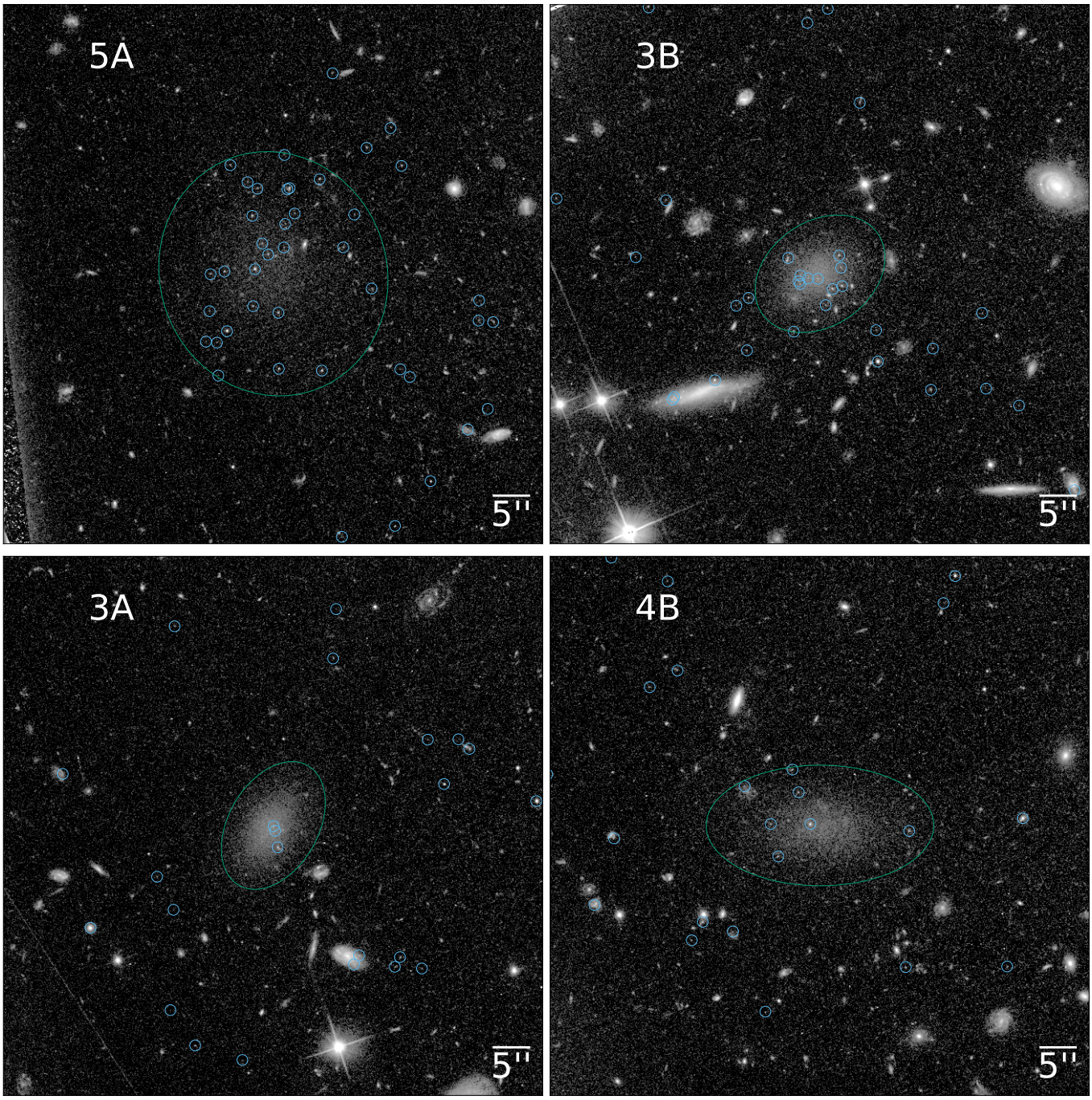


Figure 2. The GC candidates for UDGs 5A (*top left*), 3A (*bottom left*), 3B (*top right*), and 4B (*bottom right*), overlaid on the coadded F606W+F814W images. The UDGs in the top panels have significant GC detections, while those in the bottom panels do not. Each GC candidate, shown in blue, passes our optimized concentration and color cuts. The galaxy region is shown as a green ellipse which has the same size and shape as the galaxy, but extends to $2r_{\rm eff}$. Those candidates within the galaxy region are associated with the galaxy. At the distance of group A (B), $5''$ corresponds to $\sim$1.8(2.2) kpc

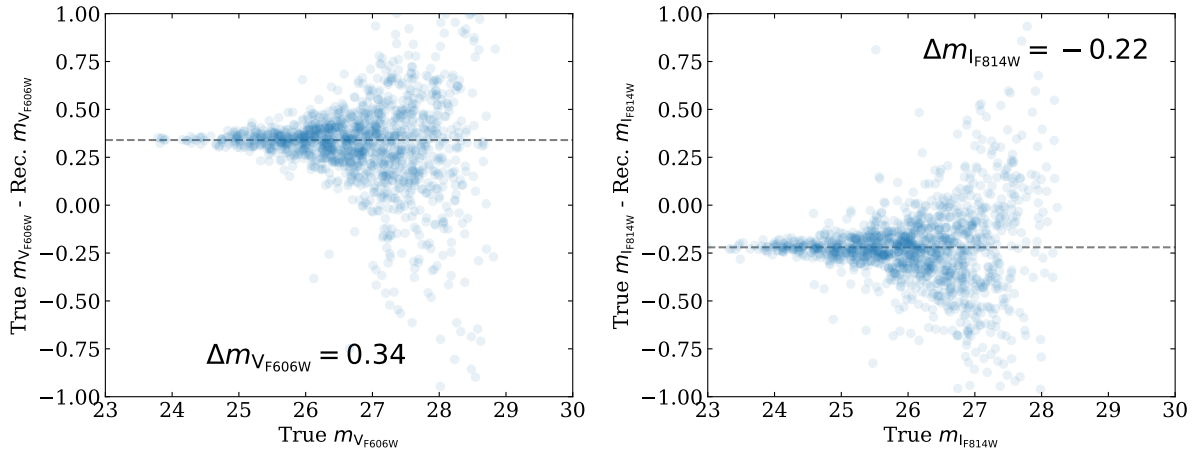


Figure 3. The scatter in our recovered magnitude for UDG 5A, assuming an initial magnitude zeropoint of 26.0. Blue scatter points shows the magnitude difference between the recovered mock GC magnitudes and the true, injected mock GC magnitudes as a function of the true magnitude. The plot on the *left* shows the magnitude error for the F606W band, while the plot on the *right* shows the same for the F814W band. We find a magnitude zeropoint shift of 0.34 mag for F606W filter and -0.22 mag for the F814W filter.

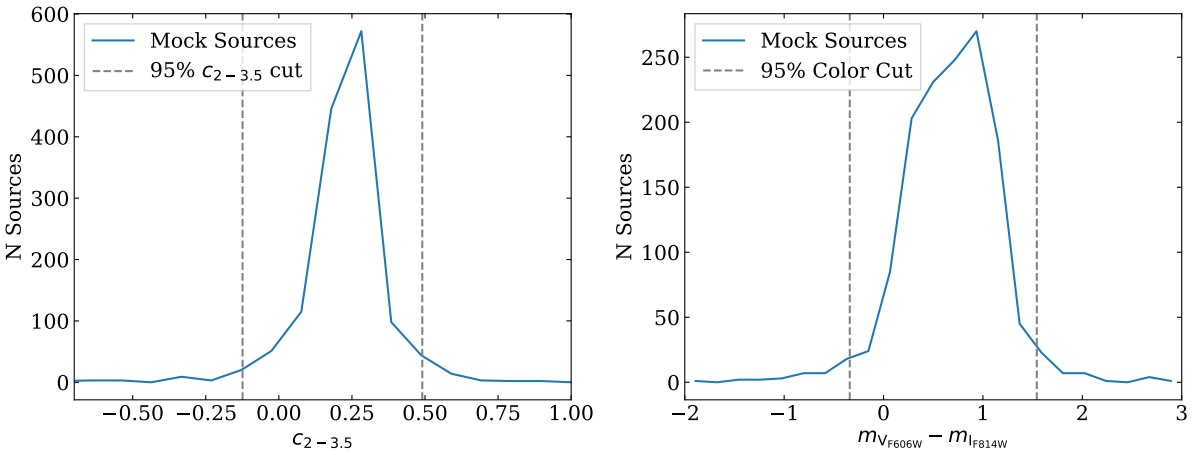


Figure 4. *left* A histogram of the UDG 5A injected mock GC concentration $c_{2-3.5}$, defined as the magnitude measured in the F606W band with a 2 pixel radius aperture subtracted from that measured with a 3.5 pixel aperture. Grey dashed lines show our 95% containment cuts. *right* A histogram of the recovered color $m_{V_{F606W}} - m_{I_{F814W}}$ for our injected mock GCs in UDG 5A. Grey dashed lines show our 95% containment cuts.

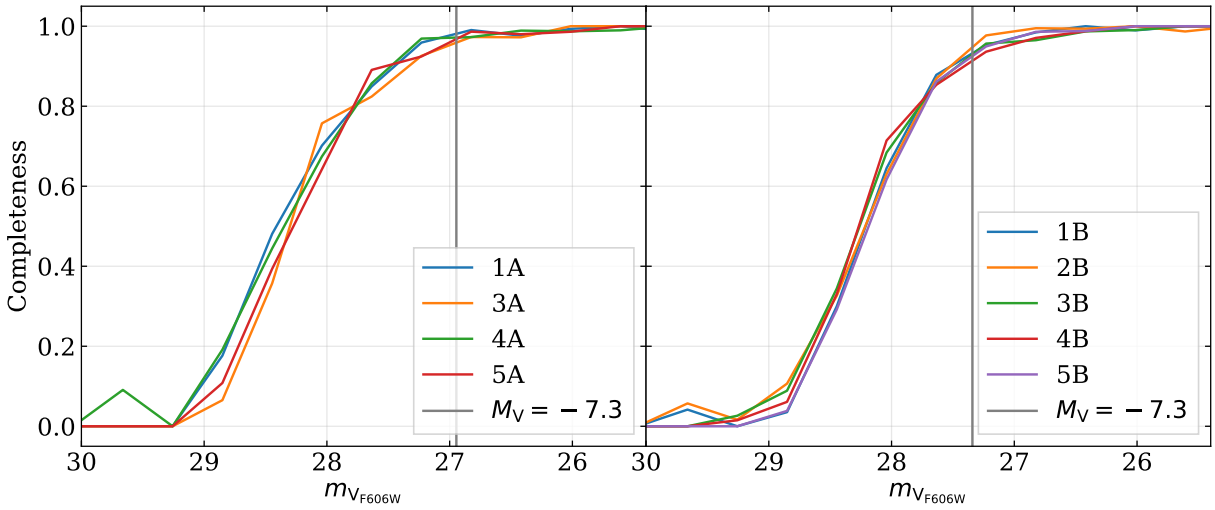


Figure 5. Completeness curves. The completeness curve as a function of F606W magnitude for group A is shown on the *left* and that for group B is shown on the *right*. In all cases, we are complete to ∼95% at the GCLF peak $M_V = -7.3$, shown as a grey vertical line.

pleteness curves and assuming that the GCLF has mean $M_V = -7.3$ and width $\sigma = 1.1$ (Miller & Lotz 2007), we expect to recover $\sim 70 - 80\%$ of the GCs in our UDGs. Thus, we will correct our observations for completeness by multiplying the observed number of GCs by $1.2-1.4$. The exact completeness corrections for each UDG are reported in Table 2. Note that we are not applying a spatial completeness correction. Previous work has suggested that such a correction would be a factor of ∼2 (e.g. van Dokkum et al. 2017; Saifollahi et al. 2020). Because of the uncertain nature of this correction, we choose to simply report the expected number of GCs within $2r_{\rm eff}$.

4. RESULTS

4.1. *Globular Cluster Detections*

In Figure 6, we show a histogram of the counts in the background regions for each UDG. We fit the background count distributions to Poisson distributions, which are shown in red. We use the Poisson distributions to assess the significance of an excess GC detection in each galaxy region. UDGs 5A and 3B show unambiguous globular cluster detections, with p-values smaller than 10^{-4}. UDG 4A has a marginally significant p-value of 0.005, so we do not consider it an unambiguous detection. In all other cases, we have non-detections.

We find the number of GCs in each UDG by subtracting the average background count from the number of galaxy GC candidates and correcting for completeness. We find that UDG 5A has $N_{\rm GC} = 26 \pm 7$, and UDG 3B has $N_{\rm GC} = 13 \pm 5$, where the reported uncertainties are entirely statistical. The remainder of our sample shows no statistically significant concentrations of GCs. The background subtracted and completeness corrected number of GCs detected in each galaxy is shown in Table 2. The completeness corrected average background for each UDG is shown in the third column.

Because the number of GCs varies with stellar and halo mass, it is standard to consider the GC specific frequency, which is the number of GCs normalized by the galaxy luminosity, $S_{\rm N} = N_{\rm GC} 10^{0.4(M_V+15)}$. We show the specific frequency for each galaxy in the fourth column of Table 2. Eight of our UDGs have $S_{\rm N} \lesssim 10$ within their uncertainties. The exception is UDG 5A with $S_{\rm N} = 50 \pm 10$.

The specific frequency is best for comparing galaxies with the same mass-to-light ratios, so we also report the T parameter, which is the stellar mass normalized number of GCs, $T = N_{\rm GC}/(M_*/10^9\,M_\odot)$. As shown in the fifth column of Table 2, UDGs 5A ($T \sim 600$) and 3B ($T \sim 200$) are the only UDGs with T significantly greater than zero.

There is a suggestion that the number of GCs correlates with halo mass (e.g. Blakeslee et al. 1997). If this correlation holds for UDGs (e.g. Harris et al. 2017), we can use our UDG GC populations to calculate GC-inferred halo masses. Using the recent calibration from Harris et al. (2017), the halo mass $M_{\rm Halo,\,GC}$ is given in units of solar masses by

$$\log\left(\frac{N_{\rm GC}}{M_{\rm Halo,\,GC}}\right) = -8.56 - 0.11\log\left(M_{\rm Halo,\,GC}\right).$$

We show upper and lower bounds on our GC-inferred UDG halo masses $M_{\rm Halo,\,GC}$ in the last column of Table 2. UDGs 5A and 3B are consistent with GC-inferred halo masses larger than $10^{11}\,M_\odot$, which may be larger

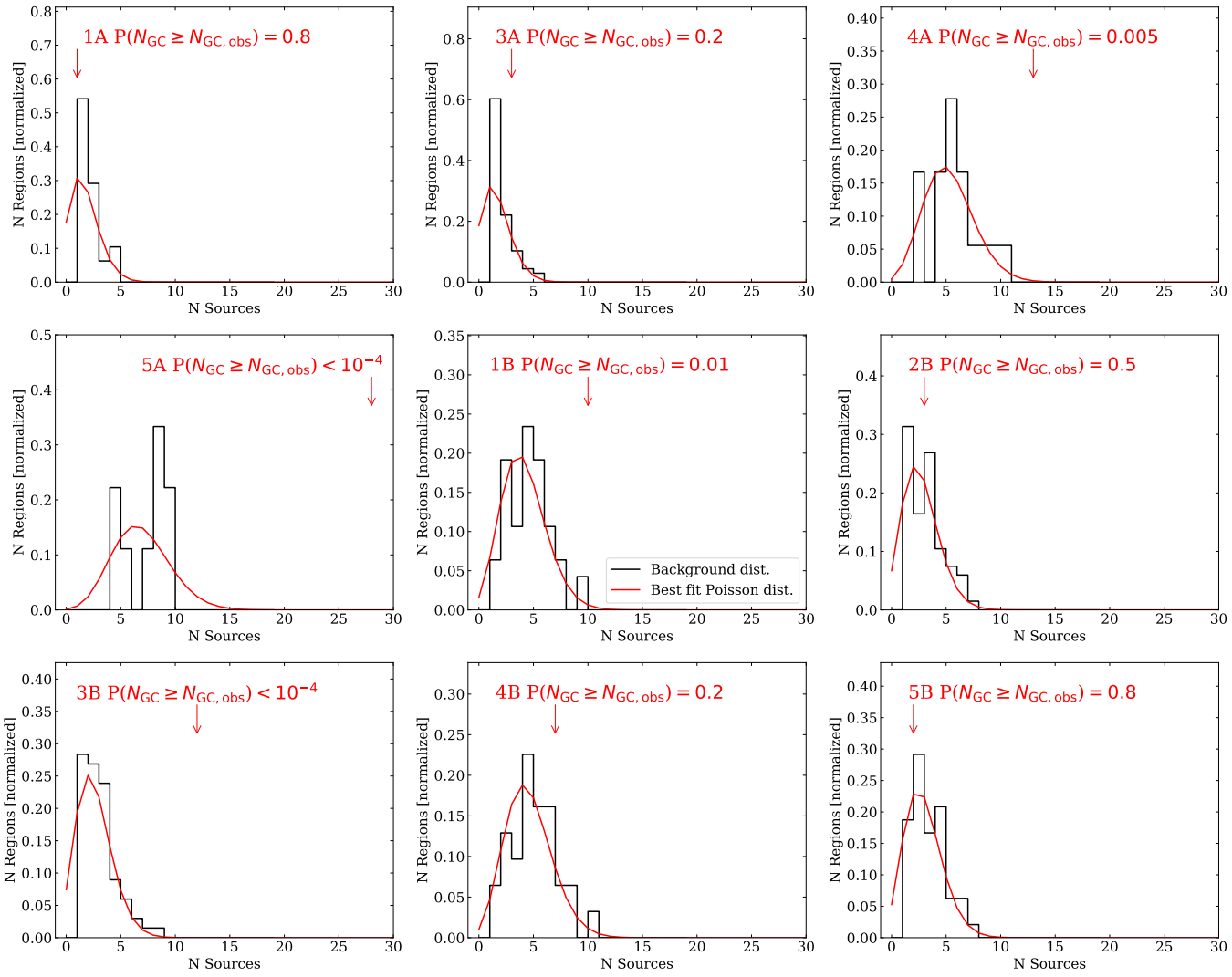


Figure 6. The number of GC candidates in the galaxy region compared to the GC candidate background for each UDG. The number of GC candidates detected in each galaxy region is shown as a red arrow. Histograms of the number of GC candidate detections in each background region are shown in black. Poisson fits to the background GC distributions are shown as red lines, and the resulting p-values for the GC detections are shown at the top of each panel. UDGs 5A and 3B show very significant detections with p-values smaller than 10^{-4}. The rest of the UDGs have insignificant detections, with p-values > 0.005.

than expected given current predictions of the UDG stellar-halo mass relation (e.g. Behroozi et al. 2019). The remainder have $M_{\rm Halo,\,GC} \lesssim 8 \times 10^{10}\,M_{\odot}$.

Finally, we consider the average colors of the globular clusters in those UDGs with significant detections. After correcting for background contamination, we find that UDG 5A has a GC color distribution with mean $\langle V-I \rangle = 0.54 \pm 0.05$ and standard deviation $\sigma_{(V-I)} = 0.13 \pm 0.1$. UDG 3B has a GC color distribution with mean $\langle V-I \rangle = 0.51 \pm 0.07$ and standard deviation $\sigma_{(V-I)} = 0.19 \pm 0.1$. In calculating the GC population parameters for each UDG, we assume a color uncertainty of $\delta(V-I) = 0.2$ on each individual GC. The mean GC colors are blue, as seen in GC systems in dwarf elliptical galaxies (Lotz et al. 2004; Georgiev et al. 2009).The colors are also consistent with the diffuse galaxy light for our sample, which is a trend that has been seen in other UDG samples (e.g. Beasley & Trujillo 2016; van Dokkum et al. 2017), albeit with small samples thus far.

4.2. *Globular Cluster Luminosity Function*

UDGs 5A and 3B both contain enough GCs to examine their GC luminosity distributions. In Figure 7, we show in black the completeness-corrected GC luminosity functions for these two UDGs. To characterize the shape and peak of the luminosity functions, we fit them

Table 2. Ultra-Diffuse Galaxy Globular Cluster properties

Galaxy	$N_{\rm GC}$	$N_{\rm bkg}$	$S_{\rm N}$	T	Completeness correction	$c_{2-3.5}$ cut	$m_{V_{F606W}} - m_{\rm I_{F814W}}$ cut	$M_{\rm Halo,\,GC}$ $[10^{10} M_\odot]$
UDG-1A	-1 ± 2	2.1 ± 0.2	-1 ± 2	-10 ± 20	1.2	$[-0.13, 0.49]$	$[-0.19, 1.45]$	$[0, 0.4]$
UDG-3A	2 ± 3	2.0 ± 0.2	3 ± 5	30 ± 60	1.2	$[-0.15, 0.48]$	$[-0.3, 1.65]$	$[0, 2]$
UDG-4A	9 ± 5	6.3 ± 0.7	13 ± 7	150 ± 80	1.2	$[-0.21, 0.49]$	$[-0.34, 1.6]$	$[2, 8]$
UDG-5A	26 ± 7	8.4 ± 1.1	50 ± 10	600 ± 200	1.2	$[-0.12, 0.49]$	$[-0.34, 1.54]$	$[11, 21]$
UDG-1B	8 ± 5	5.7 ± 0.4	7 ± 4	80 ± 50	1.4	$[-0.49, 0.59]$	$[-0.43, 1.98]$	$[1, 8]$
UDG-2B	0 ± 3	3.7 ± 0.3	1 ± 4	6 ± 50	1.4	$[-0.3, 0.54]$	$[-0.51, 1.69]$	$[0, 1.7]$
UDG-3B	13 ± 5	3.6 ± 0.3	17 ± 7	200 ± 90	1.4	$[-0.46, 0.56]$	$[-0.42, 1.77]$	$[4, 11]$
UDG-4B	3 ± 4	6.3 ± 0.5	4 ± 5	50 ± 60	1.4	$[-0.47, 0.53]$	$[-0.44, 1.93]$	$[0, 4]$
UDG-5B	-1 ± 3	4.1 ± 0.3	-10 ± 10	-70 ± 150	1.4	$[-0.33, 0.49]$	$[-0.34, 1.76]$	$[0, 0.6]$

NOTE—$N_{\rm GC}$, $S_{\rm N}$, and T have been background subtracted and completeness corrected, assuming a Gaussian GCLF with mean $M_V = -7.3$ and $\sigma = 1.1$. Error bars are entirely statistical. Negative values of $N_{\rm GC}$ are set to 0. We show the lower and upper bounds on $M_{\rm Halo,\,GC}$, calculated using the calibration from Harris et al. (2017).

to Gaussian functions. We directly fit the unbinned data using a maximum likelihood formulation which is described in Appendix A. The resulting best fit signal Gaussian is shown in blue in Figure 7. The shaded region of the plot has a completeness < 0.5. UDG 5A was best fit by a Gaussian with mean $\mu_{M_V} = -7.49 \pm 0.4$ and width $\sigma = 1.1 \pm 0.2$. UDG 3B was best fit by a Gaussian with mean $\mu_{M_V} = -7.90 \pm 0.5$ and width $\sigma = 0.7 \pm 0.4$.

5. OBSERVED TRENDS IN THE GLOBULAR CLUSTER POPULATIONS OF ULTRA-DIFFUSE GALAXIES

In the following, we will discuss the observed trends in UDGs and their GC populations. First, we will show that the GC luminosity functions of our UDGs with detections are consistent with observations of UDGs, dwarf galaxies, and high stellar mass galaxies (e.g., L_* galaxies). Then, we will show that the GC abundances in our UDGs are consistent with both dwarf galaxies and other UDGs. Finally, we will perform a covariance analysis to better understand the relationship between galaxy stellar mass, size, and GC abundance.

We will compare our observations to previous results as detailed in Table 3. These comparison samples contain dwarf galaxies, UDGs in low density environments, and UDGs in high density environments. We quote effective V-band surface brightness $\langle \mu_V \rangle$, defined as the average surface brightness within the effective radius. For all comparison samples, we report stellar masses assuming a mass-to-light ratio $(M_*/L_V)/(M_*/L_V)_\odot = 1$. We will only compare to the galaxies with $10^7 < M_*/M_\odot < 10^9$ in order to match our UDG sample.

We note that the dwarf sample from Miller & Lotz (2007), the UDG samples from Lim et al. (2018) and van Dokkum et al. (2017) are among the least biased in $N_{\rm GC}$. The galaxies in these samples were not selected for analysis because they had large GC populations. We will focus on these works in Section 6.

5.1. *The UDG GCLFs are normal*

The peak of the globular cluster luminosity function does not appear to vary significantly between galaxies. Miller & Lotz (2007) found that the GCLF of Virgo dwarf elliptical galaxies is well modelled by a Gaussian with mean $M_V = -7.3 \pm 0.1$ and width $\sigma = 1.2 \pm 0.2$. They found that the GCLF peak is $\sim$0.3 mag brighter in giant spirals and ellipticals, but the variation in GCLF peak is typically smaller than 0.3 mag within a single galaxy type.

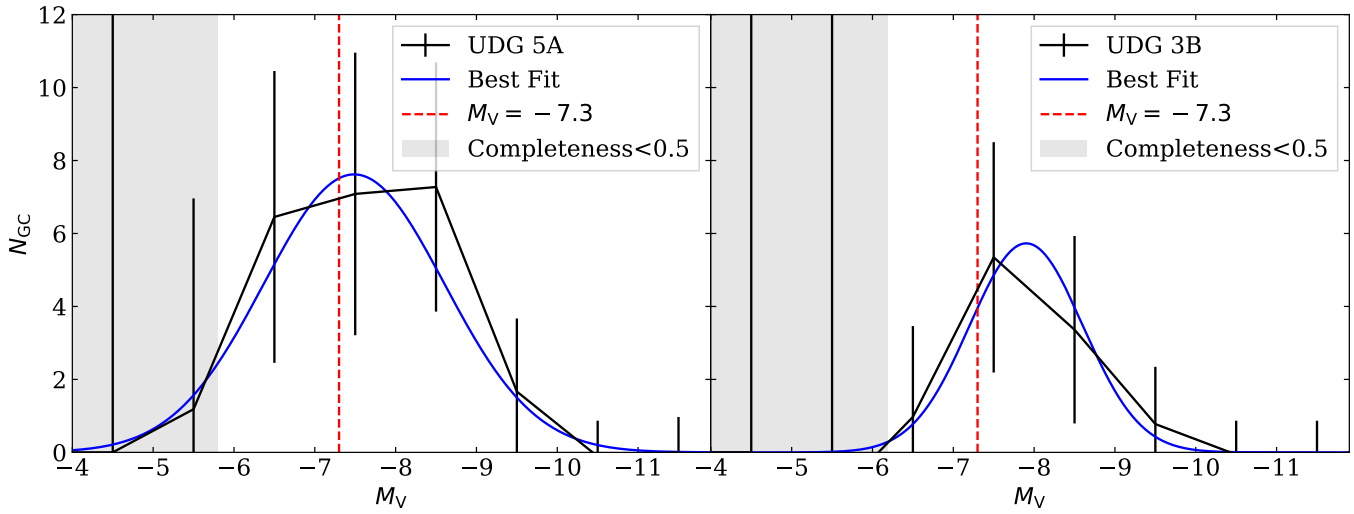


Figure 7. The globular cluster luminosity functions for UDG 5A *left* and 3B *right*. The shaded region has a completeness < 0.5. A Gaussian fit to the unbinned data is shown in blue. We find that the GCLFs have means $\mu_{M_V} = -7.49 \pm 0.4, -7.90 \pm 0.5$, and widths $\sigma = 1.1 \pm 0.2, 0.7 \pm 0.4$) for UDG 5A and 3B, respectively. The UDG GCLF peaks are both consistent with the expected $M_V = -7.3$ within $\sim 2\sigma$.

Table 3. Summary of comparison galaxy samples

Type	Environment	$\langle \mu_V \rangle$ mag arcsec^{-2}	M_* $[M_\odot]$	S_N	$M_{\rm Halo,\,GC}$ $[M_\odot]$	Refs.
Dwarf	Clusters, groups	$19-24$	$10^{7.5-9}$	1	10^{10-11}	Miller & Lotz 2007; Harris et al. 2013
UDGs	High density (clusters)	$25-28$	10^{7-8}	$0-100$	10^{10-12}	Lim et al. 2018; Beasley & Trujillo 2016 Peng & Lim 2016; van Dokkum et al. 2017 Beasley et al. 2016
UDGs	Low density (groups, isolated)	$25-28$	10^{7-8}	$0-40$	10^{10-11}	Prole et al. 2019; Román et al. 2019 van Dokkum et al. 2018b,a Danieli et al. 2019

NOTE—All numerical values are approximate. We assume a solar mass-to-light ratio.

Most studies of the UDG GCLF report peaks consistent with $M_V \sim -7.3$ (e.g. Peng & Lim 2016; Román et al. 2019; van Dokkum et al. 2017). They typically measure widths $\sigma \sim 0.8$, which is slightly narrower than those measured in dwarf ellipticals. The GCLFs for the NGC 1052 UDGs DF2 and DF4 are abnormally bright with peaks at $M_V \sim -9$ (van Dokkum et al. 2018b,a). These UDGs are also interesting because they may have small dark matter halos ($M_{\rm halo} \lesssim 10^8\,M_\odot$; Trujillo et al. 2019; Martin et al. 2018; Danieli et al. 2019).

The GCLF peaks in UDG 5A ($\mu_{M_V} \sim -7.49 \pm 0.4$) and UDG 3B ($\mu_{M_V} = -7.90 \pm 0.5$) are both consistent with Miller & Lotz (2007), as well as previous work on UDGs within $\sim 2\sigma$. Their GCLF widths are also consistent with previous UDG observations ($\sigma \sim 0.8$) and with the Miller & Lotz (2007) result. In Section 7, we will use this similarity between GCLFs in UDGs and normal dwarf and high stellar mass galaxies to argue that these galaxy types share an early GC formation history.

5.2. *GC Abundance Correlations*

In Figure 8, we compare our UDG GC specific frequencies and $T = N_{\rm GC}/(M_*/10^9)$ parameters, shown as large blue circles, to the dwarf galaxies (grey triangles), high density environment UDGs (orange squares), and UDGs in low density (group and isolated) environments (pink stars). As we mentioned, we only compare to those objects with $10^7 < M_*/M_\odot < 10^9$.

First, we consider the population of dwarfs and UDGs as a whole. In the left panel of Figure 8, we show the

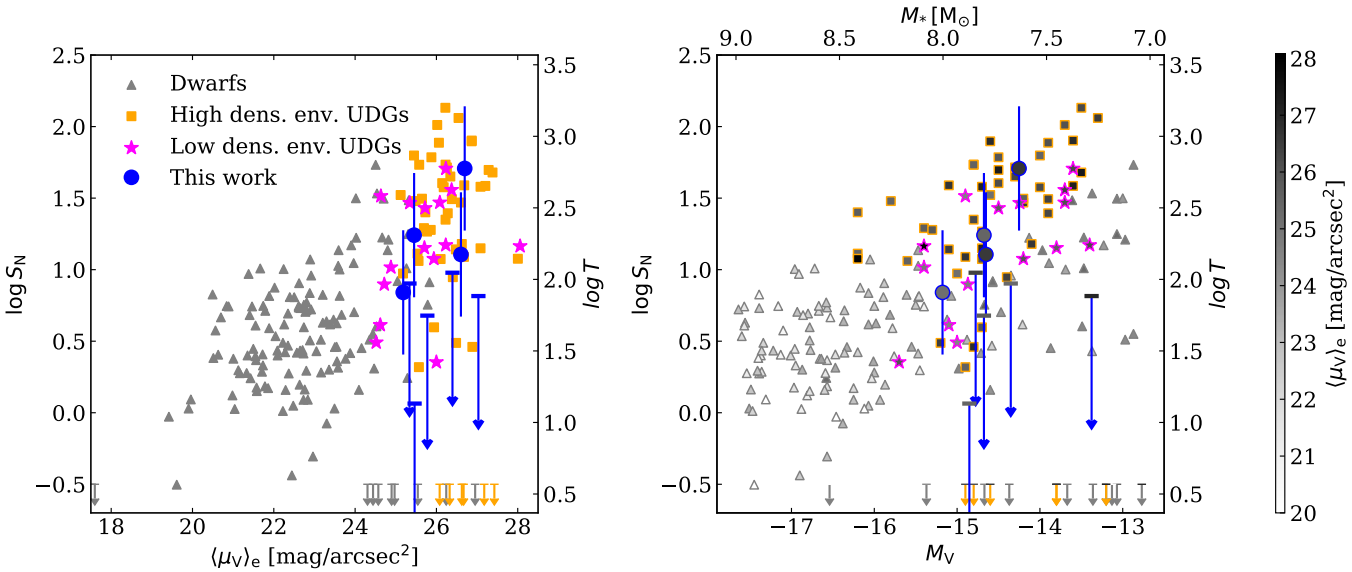


Figure 8. Properties of the UDG GC populations. The *left* panel shows the GC specific frequency (left axis) and T parameter (right axis) as a function of effective V-band surface brightness. Our UDG sample is shown as blue circles for those UDGs with detections or possible detections and upper bounds for those without detections. High density environment UDGs from Beasley & Trujillo (2016), van Dokkum et al. (2017), Peng & Lim (2016), Lim et al. (2018), and Beasley et al. (2016) are shown as orange squares, while low density environment UDGs from Román et al. (2019); Prole et al. (2019); van Dokkum et al. (2018b,a) are shown as pink stars. Dwarfs from Miller & Lotz (2007) and Harris et al. (2013) are shown as grey triangles. The *right* panel shows GC specific frequency (left axis) and T parameter (right axis) as a function of M_V (bottom axis) and stellar mass M_* (top axis), assuming a solar mass-to-light ratio (e.g. Greco et al. 2018a; Pandya et al. 2018). The shade of each marker denotes the surface brightness, with darker points having a lower surface brightness. Other than UDGs 5A and 3B, all of our UDGs are more consistent with the dwarf population and low density environment UDGs than the high density environment UDG population.

GC specific frequency and T parameter as a function of surface brightness. Those objects with non-zero specific frequencies show a possible trend of increasing specific frequency with lower surface brightness, which has been discussed by Miller & Lotz (2007) for dwarf galaxies and Lim et al. (2018) and Forbes et al. (2020) for UDGs. We choose to not directly analyze this correlation because both specific frequency and surface brightness directly depend on galaxy luminosity, which may lead to misleading correlations. Instead, we will recast it into the relationship between $N_{\rm GC}$, $r_{\rm eff}$, and M_* in Section 6.

The right panel of Figure 8 shows the specific frequency and T parameter as a function of M_V and M_*. Each data point is shaded according to its surface brightness. Like most UDGs with analyzed GC populations, the majority of our UDGs have specific frequencies more consistent with dwarf galaxies and low density environment UDGs than high density environment UDGs. UDG 3B has a slightly elevated specific frequency but is consistent with both the low density environment (pink stars) UDG population and dwarf (grey triangles) population within errors. UDG 5A shows a significantly elevated specific frequency more consistent with the high density environment (orange squares) UDGs than either the other low density environment UDGs or the dwarfs.

From the decrease in UDG GC specific frequency from high density (orange squares) environments to low density environments (pink stars), we see that there may be a correlation between UDG environment and GC abundance. We highlight this possible trend in Figure 9, which shows the UDG GC specific frequency as a function of host halo mass for those objects where host halo masses are available. The richest GC systems ($S_{\rm N} \gtrsim 70$) are still all seen in clusters. This trend with environment is tantalizing. However, given the relation between halo mass and number of subhalos, observations of a $10^{15}\,M_\odot$ cluster can sample the dwarf satellite population much better than observations of a few low-mass groups can. It is possible that we simply require a larger sample of UDGs in low density environment to reveal the rare, extremely GC-rich systems.

To naively estimate the required observations to test this environmental trend, note that ∼10% of the Coma UDGs reported in van Dokkum et al. (2017) and Lim et al. (2018) which lie in our mass range are on the extreme high tail of GC abundance, which we define as

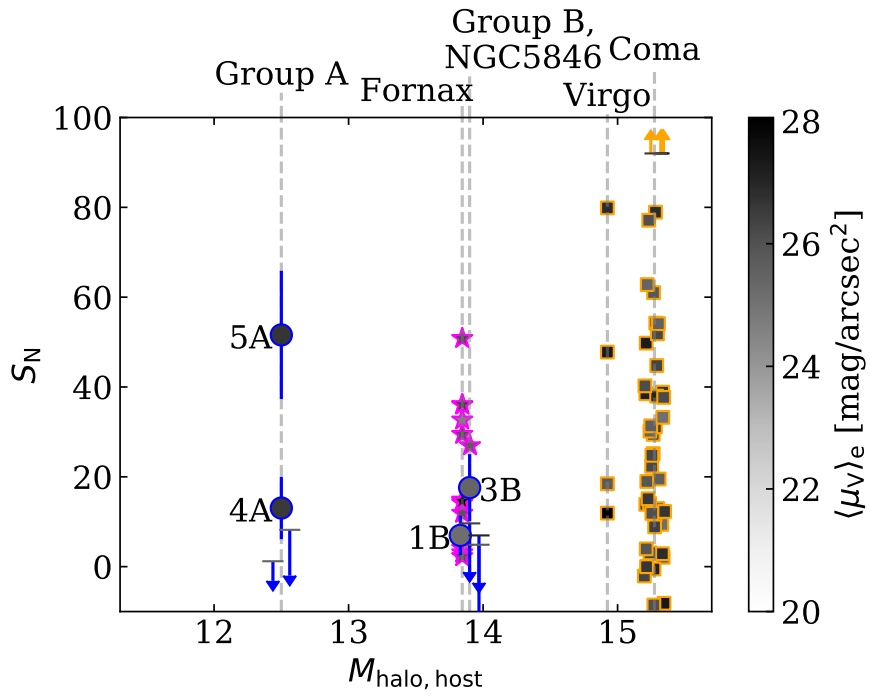


Figure 9. A comparison of GC populations for UDGs in different environments. We show the specific frequency as a function of host halo mass. The results for our group UDGs are shown as blue circles at $M_{\rm halo,host} = 10^{12.5}\,M_\odot$ (group A) and $M_{\rm halo,host} = 10^{13.7}\,M_\odot$. Arrows show upper bounds for those UDGs with no detection. UDGs in high density, cluster environments (Lim et al. 2018; Beasley et al. 2016; Beasley & Trujillo 2016; Peng & Lim 2016; van Dokkum et al. 2017) are shown as orange squares. UDGs in low density environments (Prole et al. 2019; Román et al. 2019; van Dokkum et al. 2018a,b) are shown as pink stars. Our group UDGs appear to have smaller $S_{\rm N}$ than the high density environment UDGs and the scatter in our UDG $S_{\rm N}$ also appears to be smaller than that of the high density environment UDGs, although we require a larger sample size to determine if this environmental dependence is statistically significant. However, the other UDGs outside of clusters appear consistent with our results.

$S_{\rm N} \gtrsim 100$. Due to low statistics in the extreme GC abundance regime, there are large uncertainties on this estimate of 10%, so we will instead consider the range $5-15\%$. According to Poisson statistics, we require observations of $\sim 30-80$ lower density environment UDGs to exclude with 2σ confidence the presence of UDGs with $S_N \gtrsim 100$. If we expect a given group to host 5 UDGs, we require observations of at least $6-16$ groups. While this is a very crude estimate, it highlights that more high-resolution observations of UDGs in groups would be powerful. Of course, the distribution of UDG halo mass may actually depend on environment, a possibility we discuss in Section 6.

6. THE RELATIONSHIP BETWEEN GC ABUNDANCE, GALAXY STELLAR MASS, AND GALAXY SIZE

6.1. *Covariance Analysis Methods*

In Figure 8, we see a possible trend between surface brightness and GC specific frequency, suggesting a possible relationship between stellar mass (or equivalently, luminosity), galaxy size, and GC abundance. To gain further insight into this relationship, we performed a Bayesian fit to the UDG and dwarf samples. We assumed that the joint $r_{\rm eff}$ and $N_{\rm GC}$ distribution can be described by a multivariate Gaussian, where the mean of the Gaussian depends on stellar mass M_*. Specifically, the Gaussian is described by the mean vector and covariance matrix

$$\boldsymbol{\mu} = [\,\alpha_{r_{\rm eff}} \log M_* + \pi_{r_{\rm eff}}, \alpha_{N_{\rm GC}} \log M_* + \pi_{N_{\rm GC}}\,] \quad (1)$$

$$\boldsymbol{\Sigma} = \begin{pmatrix} \sigma^2_{r_{\rm eff}} & r_{\rm cor} \times (\sigma_{r_{\rm eff}} \sigma_{N_{\rm GC}}) \\ r_{\rm cor} \times (\sigma_{r_{\rm eff}} \sigma_{N_{\rm GC}}) & \sigma^2_{N_{\rm GC}} \end{pmatrix} \quad (2)$$

Here, $r_{\rm cor} = {\rm Corr}(\log r_{\rm eff}, \log N_{\rm GC})$ is the correlation coefficient, distinct from the effective radius $r_{\rm eff}$. More-

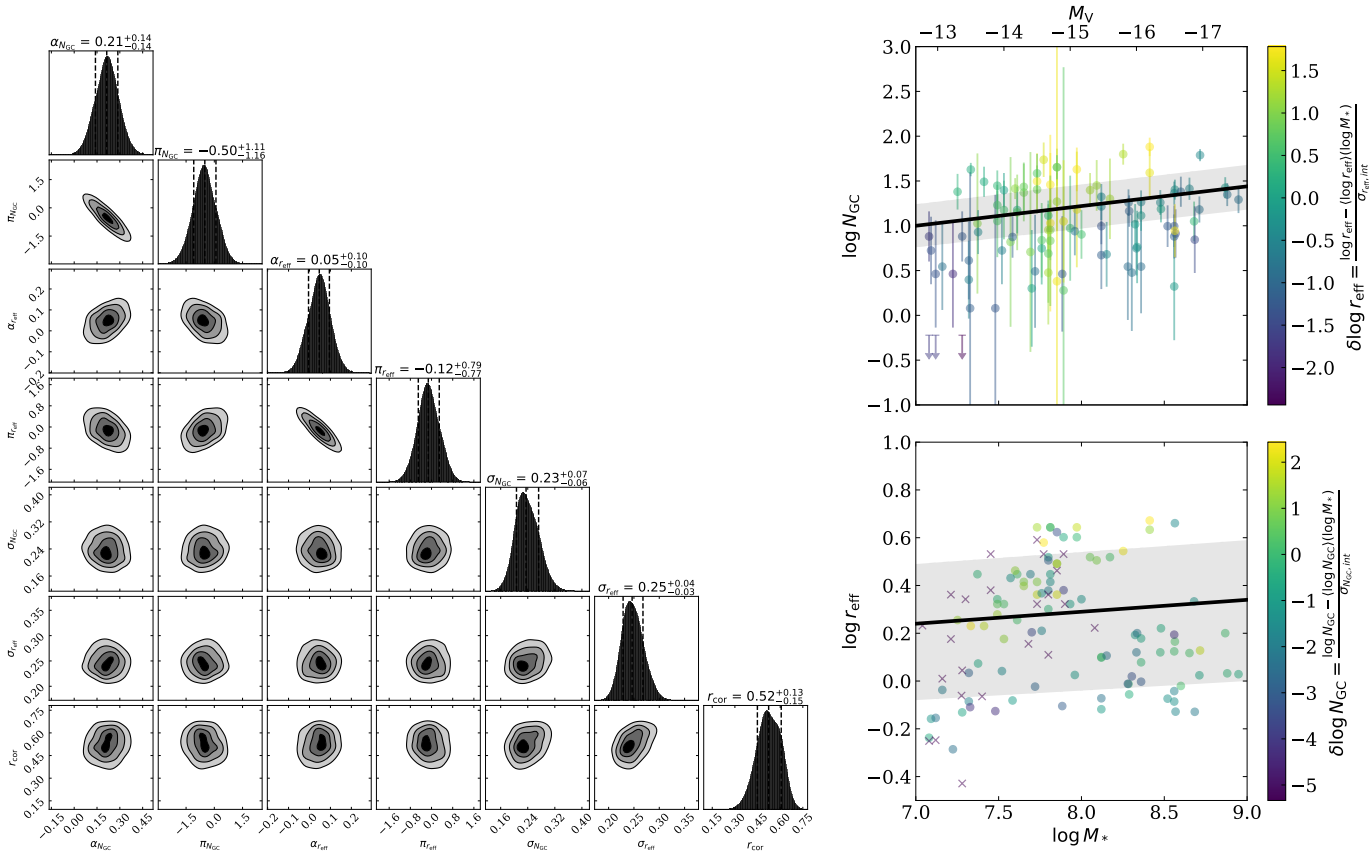


Figure 10. Posterior distribution for the covariance analysis of the relationship between stellar mass, effective radius, and globular cluster population for a sample of low mass galaxies. Relevant parameters are defined in Equation 1 and Equation 2. Prior distributions are presented in Equation 5. From the corner plot on the *left*, we see a possible linear dependence of log $N_{\rm GC}$ on log M_*, with large scatter. We do not detect any significant trend between log $r_{\rm eff}$ and log M_*. We find a significant correlation coefficient $r_{\rm cor}$. The dependence of log $N_{\rm GC}$ on log M_* is shown on the *top right*. The corresponding magnitude scale is shown on the top axis, assuming $(M_*/L_V)/(M_*/L_V)_\odot = 1$. The data are shown as a scatter plot, with each point colored by the residual error in the best fit to its effective radius. Error bars on log $N_{\rm GC}$ are shown, but the assumed errors on log M_* are suppressed for clarity. The best fit linear relationship between $N_{\rm GC}$ and M_* is shown as a black line, and the intrinsic scatter is shown as a grey band. The dependence of log $r_{\rm eff}$ on log M_* is shown on the *bottom right* in the same format as the log $N_{\rm GC}$ vs log M_* plot, but with data points are colored by their residual log $N_{\rm GC}$ error. Assumed errors on both log M_* and log $r_{\rm eff}$ are suppressed for clarity.

over, we have defined

$$\sigma_{r_{\rm eff}} = \sqrt{\sigma^2_{r_{\rm eff},intr} + \sigma^2_{r_{\rm eff},obs} + (\alpha_{\rm r_{eff}} \sigma_{M_*,obs})^2} \quad (3)$$

$$\sigma_{N_{\rm GC}} = \sqrt{\sigma^2_{N_{\rm GC},intr} + \sigma^2_{N_{\rm GC},obs} + (\alpha_{\rm N_{GC}} \sigma_{M_*,obs})^2}, \quad (4)$$

where $\sigma_{i,obs}$ is the observational uncertainty for $i \in \{\log {\rm N_{GC}}, \log {\rm r_{eff}}\}$, and $\sigma_{i,intr}$ is the intrinsic scatter in the relationship between i and $\log M_*$. The terms containing $\alpha_{\rm i}\sigma_{M_*,obs}$ account for the scatter resulting from the observational uncertainty of M_*. We assume $\sigma_{r_{\rm eff},obs} = 0.1$ dex, and we calculate $\sigma_{N_{\rm GC},obs}$ from the error reported for each $N_{\rm GC}$ measurement. We fit for both $\sigma_{r_{\rm eff},intr}$ and $\sigma_{N_{\rm GC},intr}$.

We fit this Gaussian to the dwarf sample from Miller & Lotz (2007), the UDG samples from Lim et al. (2018) and van Dokkum et al. (2017), and our UDG sample. A number of these objects have null or negative GC detections (negative detections in a given UDG arise from the statistical background subtraction). We do not input these values into our likelihood in the same way as positive detections; instead, before each likelihood evaluation, we resample these values from a Gaussian centered at zero and with a width corresponding to the reported error on that null detection. We cut off this Gaussian at zero and at $3\sigma_{\rm N_{GC}}$. The upper cutoff should not affect the results, and is to ensure that we do not randomly

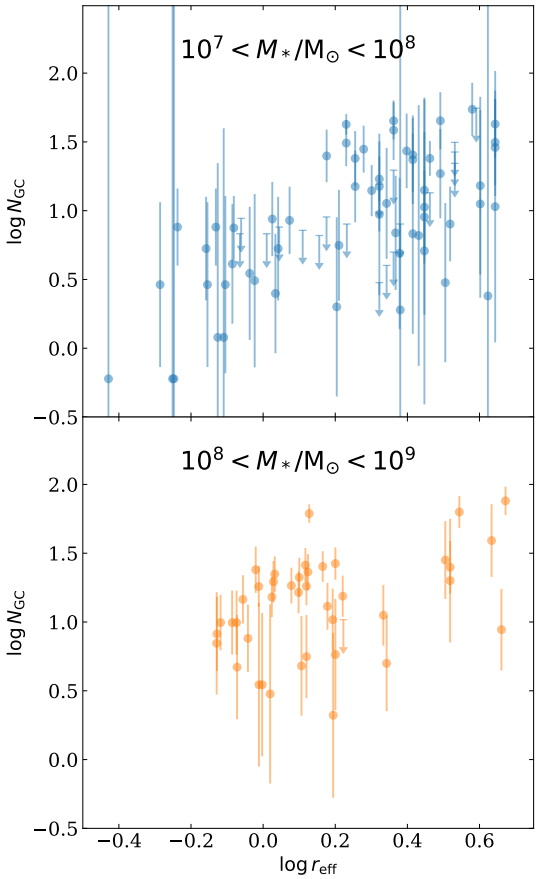


Figure 11. Correlation between GC abundance and effective radius. The *top* panel shows the dependence of log N_{GC} on log r_{eff} for all UDGs and dwarf galaxies with low stellar masses $10^7 < M_*/M_\odot < 10^8$. Arrows denote the upper 2σ limit on log N_{GC} for galaxies with null GC detections. The *bottom* panel shows the same for galaxies with higher stellar masses $10^8 < M_*/M_\odot < 10^9$. The positive correlation can be clearly seen for galaxies in the higher mass bin (*bottom* panel), and is marginally visible in the lower mass bin (*top* panel).

select an extremely large value of N_{GC}, which is improbable, but would increase our computation time.

We evaluate our likelihood using the `dynesty` sampler (Speagle 2020). We assume heaviside priors with the following limits:

$$\begin{gathered}\alpha_{r_{\rm eff}} \in [-1,1],\ \pi_{r_{\rm eff}} \in [-3,3],\ \sigma_{r_{\rm eff}} \in (0,3],\\ \alpha_{N_{\rm GC}} \in [-1,1],\ \pi_{N_{\rm GC}} \in [-3,3],\ \sigma_{N_{\rm GC}} \in (0,3],\\ r_{\rm cor} \in [-1,1]\end{gathered} \quad (5)$$

We run `dynesty` until it reaches the stopping criteria of $\Delta \log Z = 3$. In Figure 10, we show the resulting posterior space and median-best fit mass-size and GC-stellar mass relations. We find a weak linear relationship

$$\log\ N_{\rm GC} = (0.21^{+0.14}_{-0.14}) \log\ M_* + (-0.50^{+1.11}_{-1.16}), \quad (6)$$

with intrinsic scatter $\sigma = 0.23^{+0.07}_{-0.06}$. We do not find a significant mass-size relationship

$$\log\ r_{\rm eff} = (0.05^{+0.10}_{-0.10}) \log\ M_* + (-0.12^{+0.79}_{-0.77}),$$

with intrinsic scatter, $\sigma = 0.25^{+0.04}_{-0.03}$. We see a large correlation coefficient $r_{\rm cor} = 0.52^{+0.13}_{-0.15}$ between log N_{GC} and log $r_{\rm eff}$. These relations and correlations can be seen in the left panel of Figure 10, where we show log N_{GC} vs. log M_* and log $r_{\rm eff}$ vs. log M_*. The color of each point in the upper (lower) panel corresponds to the residual error $\delta \log r_{\rm eff}$ ($\delta \log N_{GC}$). There is an increase in $\delta \log N_{GC}$ with larger log $r_{\rm eff}$ and likewise in $\delta \log r_{\rm eff}$ with larger log N_{GC}.

6.2. *The $N_{GC} - r_{\rm eff}$ correlation*

In Figure 11, we show the relationship between log N_{GC} and log $r_{\rm eff}$ in two stellar mass bins, $10^7 < M_*/M_\odot < 10^8$ and $10^8 < M_*/M_\odot < 10^9$. The following discussion will explore possible origins of this relationship. We will first consider baryonic processes which could modify both galaxy size and GC abundance. Then, we will discuss an alternate scenario where galaxy size and GC abundance mutually depend on halo-related parameters. Throughout this discussion, we will assume that the high number of GCs per unit stellar mass in dwarf galaxies is evidence for an underlying relationship between GC abundance and halo mass (e.g. Harris et al. 2013), although this relation may or may not hold (e.g. El-Badry et al. 2019). Throughout, we also favor scenarios in which the formation of GCs in UDGs and higher surface brightness dwarfs are similar, given that their GCLFs are similar.

Since we assume an $N_{GC} - M_{\rm halo}$ relation at low stellar masses, the large scatter in UDG GC populations corresponds to a large scatter in UDG halo masses. This suggests either that the SHMR has large scatter in $M_{\rm halo}$ at fixed stellar mass, for low stellar masses, or that low stellar mass galaxies cannot be treated as a single, continuous population. Unless stated otherwise we will assume large scatter in the SHMR at fixed stellar mass. Because of the large scatter in the observed $N_{GC} - M_*$ relation and in the assumed $N_{GC} - M_{\rm halo}$ relation, there is room for large scatter in $M_{\rm halo}$ at fixed M_* while preserving the halo/stellar mass-N_{GC} relations. Towards the end of our discussion, we will briefly mention an alternate scenario where the $M_{\rm halo} \lesssim 10^{11}\,M_\odot$ UDGs follow a standard SHMR, while some special physics forms the $M_{\rm halo} \gtrsim 10^{11}\,M_\odot$ UDGs.

6.2.1. *Baryonic Processes*

A possible explanation of the $N_{GC} - r_{\rm eff}$ correlation is that the GC abundance and radius of a galaxy are

both affected by the same baryonic process during the course of the galaxy's evolution. In particular, internal feedback can cause a galaxy to puff up (Di Cintio et al. 2017), and may also be able to increase the GC formation efficiency (Ma et al. 2020). Alternatively, mergers may disturb the baryonic content of galaxies in a way that can both increase galaxy size (Wright et al. 2020), and modify GC formation efficiency and survival rate (Kruijssen 2014). However, these mechanisms raise the question: does such baryonic physics affect the GCLF? It is observed that the shape and peak of the GCLF are similar in UDGs and dwarf ellipticals, and since it is thought that GC disruption shapes the GCLF (e.g. Kruijssen 2014), that disruption must operate in the same way in these galaxy types. It is difficult to think of a baryonic process which would increase a galaxy's size and GC abundance without modifying GC disruption and, consequently, the GCLF. Determining if such a mechanism exists will require further study, on varied feedback levels and merger histories on the GCLF, for example.

6.2.2. *Halo mass connection*

It may be easier to devise mechanisms that can generate the $N_{\rm GC} - r_{\rm eff}$ correlation without modifying the GCLF if we do not directly rely on complex baryonic processes. In particular, the GC abundance and galaxy size may mutually depend on properties of the galaxy dark matter halo. Such a mutual dependence does not contradict any of our observations because of our assumption of large scatter in the SHMR at low stellar mass. Specifically, given the large scatter in $M_{\rm halo}$ at fixed M_*, there could be a correlation between $M_{\rm halo}$ and $r_{\rm eff}$ but no observable correlation between $r_{\rm eff}$ and M_*. Similarly, the dependence of $N_{\rm GC}$ on a halo-related parameter would remain consistent with our observed $N_{\rm GC} - M_*$ relation. As a specific example of a mutual halo dependency, Kravtsov (2013) and Harris et al. (2013) have suggested that in the high stellar mass regime $r_{\rm eff}$ and $N_{\rm GC}$, respectively, may depend on the virial radius. It is possible that this mutual dependence could extrapolate to the low stellar mass regime.

Alternatively, we can remove the assumption of large scatter in the SHMR at low stellar masses, meaning that normal dwarfs can have a narrow range of halo mass at fixed stellar mass (e.g., 0.2 dex; Garrison-Kimmel et al. 2016), but UDGs have a different distribution in $M_{\rm halo}$. Forbes et al. (2020) put forward a scenario like this, in which one population of UDGs could form with $M_{\rm halo} \lesssim 10^{11}\,M_\odot$ but large sizes ($r_{\rm eff} > 1.5$ kpc) if they inhabit high angular momentum halos or experienced more extreme feedback (Carleton et al. 2019; Liao et al. 2019; Di Cintio et al. 2017; Tremmel et al. 2019). On the other hand, a special class of UDGs with $M_{\rm halo} \gtrsim 10^{11}\,M_\odot$ could have formed as failed L_* galaxies (van Dokkum et al. 2017). The UDGs with $M_{\rm halo} \lesssim 10^{11}\,M_\odot$ could be consistent with, e.g., an extrapolation of a standard SHMR and would have normal GC abundances given their stellar masses (e.g. Garrison-Kimmel et al. 2016). In contrast, the $M_{\rm halo} \gtrsim 10^{11}\,M_\odot$ UDGs would have much lower stellar-to-halo mass ratios which would not satisfy a standard SHMR and would result in GC abundances which are abnormally high given the stellar masses of those UDGs.

7. SUMMARY AND FUTURE WORK

We have studied the GC populations of nine UDGs in group environments and with surface brightnesses $\langle\mu_V\rangle \approx 25-28$ mag arcsec^{-2} and effective radii $r_{\rm eff} \sim 2.5-3.5$ kpc. We also have examined trends of GC populations in UDGs more broadly. Our main conclusions are:

- The bulk (7/9) of our lower-density environment UDGs have GC abundances ($S_{\rm N} \lesssim 10$) consistent with normal dwarf ellipticals.
- Two of our UDGs, UDGs 5A and 3B, have more GCs than expected for their stellar mass. They each have a GCLF with both peak and width consistent with the GCLFs in normal dwarf and high stellar mass galaxies and in other UDGs.
- The most GC-rich ($S_{\rm N} \gtrsim 70$) UDGs so far have been found in the densest environments. Future observations of UDG GC populations in group environments are required to constrain the presence of such objects at lower densities.
- Combining well-defined UDG and dwarf elliptical samples, we see a possible positive dependence between $N_{\rm GC}$ and M_* (slope $= 0.21^{+0.14}_{-0.14}$). We do not see a significant stellar mass-size relation (slope $= 0.05^{+0.10}_{-0.10}$).
- We find a positive correlation between $N_{\rm GC}$ and $r_{\rm eff}$ at fixed stellar mass ($r_{\rm cor} = 0.52^{+0.13}_{-0.15}$), which is similar to the surface brightness-$N_{\rm GC}$ relation that has been noted in the literature. Possible origins for this correlation include a mutual dependence of $N_{\rm GC}$ and $r_{\rm eff}$ on properties of the galaxy dark matter halo or a connection through the baryonic processes such as those involved in internal feedback or caused by galaxy mergers.

Further constraints on these observed trends, in particular on the possible environmental trend and the correlation between GC abundance and galaxy size, will require further observational and theoretical work. First, we would benefit from theoretical work modelling the effects of strong feedback, extreme variations in merger history, and enhanced/reduced star formation on GC formation. From the observational side, GC-independent halo mass constraints (e.g., dynamical measurements) would also provide a very powerful constraint on the discussed models. In particular, it would

allow us to evaluate the validity of the $N_{\rm GC} - M_{\rm halo}$ relation in the UDG regime, which has been called into question by some theoretical work (e.g. El-Badry et al. 2019).

Moreover, we require a better understanding of the space density of galaxies as a function of surface brightness. The low stellar mass galaxy samples which we consider have unknown number densities, and they are not volume complete, which makes it difficult to define their SHMR. This incompleteness could also lead to an artificially flat mass-size relation, although Danieli & van Dokkum (2019) also found no mass-size relation in their volume-complete sample of Coma cluster galaxies.

We have not accounted for the uncertainties in the distances to our UDGs, which could modify our constraints on $N_{\rm GC}$. In future work, Greco (in prep.) will measure the redshift distribution of the Greco et al. (2018b) sample, enabling statistical distance corrections.

Our results are also subject to the assumption of a constant mass-to-light ratio $(M_*/L_V)/(M_*/L_V)_\odot = 1$. Our covariance analysis results could be explained if, for example, there is a systematic trend in mass-to-light ratio with size. In the future, a more rigorous determination of stellar mass is necessary to assess the true relationship between GC abundance, galaxy stellar mass, and galaxy size. For example, multi-band SED fitting or spectroscopic fitting in the LSB regime, although difficult, could provide the necessary stellar mass measurements (e.g. Barbosa et al. 2020; Ferré-Mateu et al. 2018; Pandya et al. 2018; Greco et al. 2018a; Gu et al. 2018).

Finally, most low stellar mass galaxy samples, including ours, are biased towards high density environments. This density bias may further modify the mass-size relation, and may skew the SHMR. Further observations of UDGs in a range of environments and constraints on their GC populations are critical to verify that the discussed trends are real. In future work, we hope to begin reducing the environmental incompleteness of the UDG sample by characterizing the GC populations in a much larger LSBG sample from the Greco et al. (2018b) catalog, encompassing galaxies in a wide range of environments.

ACKNOWLEDGMENTS

We'd like to thank Michael Strauss for contributions to the *HST* proposal. We'd also like to thank the anonymous referee for helpful comments. J.P.G. is supported by an NSF Astronomy and Astrophysics Postdoctoral Fellowship under award AST-1801921.

Support for this work was provided by NASA through grant number 15277 from the Space Telescope Science Institute, which is operated by AURA, Inc., under NASA contract NAS 5-26555.

Facilities: HST(ACS/WFC), Subaru(HSC)

Software: Astropy (Robitaille et al. 2013; Astropy Collaboration et al. 2018), Drizzlepac (Team & Team 2012; Avila et al. 2014), Matplotlib (Hunter 2007), NumPy (Oliphant & Millma 2006; Van Der Walt et al. 2011), Pandas (Team 2020; McKinney 2010), SciPy (Virtanen et al. 2020), statsmodels (Seabold & Perktold 2010), PhotUtils (Bradley et al. 2019), dynesty (Speagle 2020; Skilling 2004, 2006)

REFERENCES

Abraham, R. G., & van Dokkum, P. G. 2014, Publications of the Astronomical Society of the Pacific, 126, 55, doi: 10.1086/674875

Aihara, H., Armstrong, R., Bickerton, S., et al. 2018, PASJ, 70, S8, doi: 10.1093/PASJ/PSX081

Amorisco, N. C., & Loeb, A. 2016, Monthly Notices of the Royal Astronomical Society: Letters, 459, L51, doi: 10.1093/mnrasl/slw055

Amorisco, N. C., Monachesi, A., Agnello, A., & White, S. D. M. 2016, Monthly Notices of the Royal Astronomical Society, 475, 4235, doi: 10.1093/mnras/sty116

Astropy Collaboration, Price-Whelan, A. M., Sip\H ocz, B. M., et al. 2018, \aj, 156, 123, doi: 10.3847/1538-3881/aabc4f

Avila, R. J., Hack, W., Cara, M., et al. 2014. http://arxiv.org/abs/1411.5605

Barbosa, C. E., Zaritsky, D., Donnerstein, R., et al. 2020, The Astrophysical Journal Supplement Series, 247, 46, doi: 10.3847/1538-4365/ab7660

Beasley, M. A., Romanowsky, A. J., Pota, V., et al. 2016, The Astrophysical Journal, 819, L20, doi: 10.3847/2041-8205/819/2/l20

Beasley, M. A., & Trujillo, I. 2016, The Astrophysical Journal, 830, 23, doi: 10.3847/0004-637x/830/1/23

Behroozi, P., Wechsler, R. H., Hearin, A. P., & Conroy, C. 2019, Monthly Notices of the Royal Astronomical Society, 488, 3143, doi: 10.1093/mnras/stz1182

Blakeslee, J. P., Tonry, J. L., & Metzger, M. R. 1997, The Astronomical Journal, 114, 482, doi: 10.1086/118488

Bosch, J., Armstrong, R., Bickerton, S., et al. 2018, PASJ, 70, S5, doi: 10.1093/PASJ/PSX080

Bradley, L., Sipőcz, B., Robitaille, T., et al. 2019, Zenodo, doi: 10.5281/ZENODO.3568287

Cao, J.-z., Tinker, J. L., Mao, Y.-Y., & Wechsler, R. H. 2019. http://arxiv.org/abs/1910.03605

Carleton, T., Errani, R., Cooper, M., et al. 2019, Monthly Notices of the Royal Astronomical Society, 485, 382, doi: 10.1093/mnras/stz383

Conselice, C. J., Gallagher, J. S., & Wyse, R. F. G. 2003, The Astronomical Journal, 125, 66, doi: 10.1086/345385

Dalcanton, J., Spergel, D. N., Gunn, J. E., Schmidt, M., & Schneider, D. P. 1997, The Astronomical Journal, 114, 2178, doi: 10.1086/118639

Danieli, S., & van Dokkum, P. 2019, The Astrophysical Journal, 875, 155, doi: 10.3847/1538-4357/ab14f3

Danieli, S., van Dokkum, P., Abraham, R., et al. 2019. http://arxiv.org/abs/1910.07529

Di Cintio, A., Brook, C. B., Dutton, A. A., et al. 2017, Monthly Notices of the Royal Astronomical Society: Letters, 466, L1, doi: 10.1093/mnrasl/slw210

Drlica-Wagner, A., Bechtol, K., Mau, S., et al. 2020, The Astrophysical Journal, 893, 47, doi: 10.3847/1538-4357/ab7eb9

Ebrahimi, H., Sollima, A., Haghi, H., Baumgardt, H., & Hilker, M. 2020, Monthly Notices of the Royal Astronomical Society, 494, 4226, doi: 10.1093/mnras/staa969

El-Badry, K., Quataert, E., Weisz, D. R., Choksi, N., & Boylan-Kolchin, M. 2019, Monthly Notices of the Royal Astronomical Society, 482, 4528, doi: 10.1093/mnras/sty3007

El-Badry, K., Wetzel, A., Geha, M., et al. 2016, ApJ, 820, 131, doi: 10.3847/0004-637X/820/2/131

Ferré-Mateu, A., Alabi, A., Forbes, D. A., et al. 2018, Monthly Notices of the Royal Astronomical Society, 479, 4891, doi: 10.1093/mnras/sty1597

Forbes, D. A., Alabi, A., Romanowsky, A. J., Brodie, J. P., & Arimoto, N. 2020. http://arxiv.org/abs/2001.10031

Forbes, D. A., Read, J. I., Gieles, M., & Collins, M. L. 2018, Monthly Notices of the Royal Astronomical Society, 481, 5592, doi: 10.1093/MNRAS/STY2584

Garrison-Kimmel, S., Bullock, J. S., Boylan-Kolchin, M., & Bardwell, E. 2016, doi: 10.1093/mnras/stw2564

Georgiev, I. Y., Hilker, M., Puzia, T. H., Goudfrooij, P., & Baumgardt, H. 2009, Monthly Notices of the Royal Astronomical Society, 396, 1075, doi: 10.1111/j.1365-2966.2009.14776.x

Greco, J. in prep.

Greco, J., Greco, & Johnny. 2017, hst, 15277

Greco, J. P., Goulding, A. D., Greene, J. E., et al. 2018a, The Astrophysical Journal, 866, 112, doi: 10.3847/1538-4357/aae0f4

Greco, J. P., Greene, J. E., Strauss, M. A., et al. 2018b, The Astrophysical Journal, 857, 104, doi: 10.3847/1538-4357/aab842

Gu, M., Conroy, C., Law, D., et al. 2018, The Astrophysical Journal, 859, 37, doi: 10.3847/1538-4357/aabbae

Harris, W. E., Blakeslee, J. P., & Harris, G. L. H. 2017, The Astrophysical Journal, 836, 67, doi: 10.3847/1538-4357/836/1/67

Harris, W. E., Harris, G. L., & Alessi, M. 2013, Astrophysical Journal, 772, doi: 10.1088/0004-637X/772/2/82

Harris, W. E., & van den Bergh, S. 1981, The Astronomical Journal, 86, 1627, doi: 10.1086/113047

Hunter, J. D. 2007, Computing in Science and Engineering, 9, 99, doi: 10.1109/MCSE.2007.55

Impey, C., Bothun, G., & Malin, D. 1988, The Astrophysical Journal, 330, 634, doi: 10.1086/166500

Jester, S., Schneider, D. P., Richards, G. T., et al. 2005, doi: 10.1086/432466

Jiang, F., Dekel, A., Freundlich, J., et al. 2019, Monthly Notices of the Royal Astronomical Society, 487, 5272, doi: 10.1093/mnras/stz1499

Koda, J., Yagi, M., Yamanoi, H., & Komiyama, Y. 2015, The Astrophysical Journal, 807, L2, doi: 10.1088/2041-8205/807/1/L2

Kovács, O. E., Bogdán, Á., & Canning, R. E. A. 2019, The Astrophysical Journal, 879, L12, doi: 10.3847/2041-8213/ab2916

Kovacs, O. E., Bogdan, A., & Canning, R. E. A. 2020. http://arxiv.org/abs/2004.11388

Kravtsov, A. V. 2013, Astrophysical Journal Letters, 764, L31, doi: 10.1088/2041-8205/764/2/L31

Krist, J. E., Hook, R. N., & Stoehr, F. 2011, in Optical Modeling and Performance Predictions V, Vol. 8127 (SPIE), 81270J, doi: 10.1117/12.892762

Kruijssen, J. M. D. 2014, Classical and Quantum Gravity, 31, 244006, doi: 10.1088/0264-9381/31/24/244006

—. 2015, Monthly Notices of the Royal Astronomical Society, 454, 1658, doi: 10.1093/mnras/stv2026

Lee, J. H., Kang, J., Lee, M. G., & Jang, I. S. 2020, The Astrophysical Journal, 894, 75, doi: 10.3847/1538-4357/ab8632

Leisman, L., Haynes, M. P., Janowiecki, S., et al. 2017, The Astrophysical Journal, 842, 133, doi: 10.3847/1538-4357/aa7575

Liang, C. J., Kravtsov, A. V., & Agertz, O. 2016, \mnras, 458, 1164, doi: 10.1093/mnras/stw375

Liao, S., Gao, L., Frenk, C. S., et al. 2019, Monthly Notices of the Royal Astronomical Society, 490, 5182, doi: 10.1093/mnras/stz2969

Lim, S., Peng, E. W., Côté, P., et al. 2018, The Astrophysical Journal, 862, 82, doi: 10.3847/1538-4357/aacb81

Lotz, J. M., Miller, B. W., & Ferguson, H. C. 2004, The Astrophysical Journal, 613, 262, doi: 10.1086/422871

Ma, X., Grudić, M. Y., Quataert, E., et al. 2020, Monthly Notices of the Royal Astronomical Society, 493, 4315, doi: 10.1093/mnras/staa527

Martin, N. F., Collins, M. L. M., Longeard, N., & Tollerud, E. 2018, The Astrophysical Journal, 859, L5, doi: 10.3847/2041-8213/aac216

McKinney, W. 2010, Proceedings of the 9th Python in Science Conference

Miller, B. W., & Lotz, J. M. 2007, The Astrophysical Journal, 670, 1074, doi: 10.1086/522323

Oliphant, T., & Millma, J. k. 2006, A guide to NumPy, doi: DOI:10.1109/MCSE.2007.58

Pandya, V., Romanowsky, A. J., Laine, S., et al. 2018, The Astrophysical Journal, 858, 29, doi: 10.3847/1538-4357/aab498

Peng, E. W., & Lim, S. 2016, The Astrophysical Journal, 822, L31, doi: 10.3847/2041-8205/822/2/l31

Peng, E. W., Jordán, A., Côté, P., et al. 2008, The Astrophysical Journal, 681, 197, doi: 10.1086/587951

Peng, E. W., Ferguson, H. C., Goudfrooij, P., et al. 2011, Astrophysical Journal, 730, doi: 10.1088/0004-637X/730/1/23

Piña, P. E. M., Aguerri, J. A. L., Peletier, R., et al. 2019, doi: 10.1093/mnras/stz238

Prole, D. J., Hilker, M., Van Der Burg, R. F., et al. 2019, Monthly Notices of the Royal Astronomical Society, 484, 4865, doi: 10.1093/mnras/stz326

Robitaille, T. P., Tollerud, E. J., Greenfield, P., et al. 2013, Astronomy and Astrophysics, 558, doi: 10.1051/0004-6361/201322068

Román, J., Beasley, M. A., Ruiz-Lara, T., & Valls-Gabaud, D. 2019, Monthly Notices of the Royal Astronomical Society, 486, 823, doi: 10.1093/mnras/stz835

Román, J., & Trujillo, I. 2017, Monthly Notices of the Royal Astronomical Society, 468, 4039, doi: 10.1093/mnras/stx694

Saifollahi, T., Trujillo, I., Beasley, M. A., Peletier, R. F., & Knapen, J. H. 2020. http://arxiv.org/abs/2006.14630

Sandage, A., & Binggeli, B. 1984, The Astronomical Journal, 89, 919, doi: 10.1086/113588

Seabold, S., & Perktold, J. 2010, in 9th Python in Science Conference

Secker, J., & Harris, W. E. 1993, The Astronomical Journal, 105, 1358, doi: 10.1086/116515

Sifón, C., van der Burg, R. F., Hoekstra, H., Muzzin, A., & Herbonnet, R. 2018, Monthly Notices of the Royal Astronomical Society, 473, 3747, doi: 10.1093/mnras/stx2648

Skilling, J. 2004, in AIPC, Vol. 735 (AIP Publishing), 395–405, doi: 10.1063/1.1835238

Skilling, J. 2006, Bayesian Analysis, 1, 833, doi: 10.1214/06-BA127

Speagle, J. S. 2020, Monthly Notices of the Royal Astronomical Society, 493, 3132, doi: 10.1093/mnras/staa278

Team, S. D., & Team, S. D. 2012, ascl, ascl:1212.011

Team, T. p. d. 2020, Pandas-dev/pandas: Pandas, doi: 10.5281/zenodo.3509134

Toloba, E., Lim, S., Peng, E., et al. 2018, The Astrophysical Journal, 856, L31, doi: 10.3847/2041-8213/aab603

Tremmel, M., Wright, A. C., Brooks, A. M., et al. 2019. http://arxiv.org/abs/1908.05684

Trujillo, I., Beasley, M. A., Borlaff, A., et al. 2019, Monthly Notices of the Royal Astronomical Society, 486, doi: 10.1093/mnras/stz771

Van Der Burg, R. F., Muzzin, A., & Hoekstra, H. 2016, Astronomy and Astrophysics, 590, doi: 10.1051/0004-6361/201628222

Van Der Burg, R. F., Hoekstra, H., Muzzin, A., et al. 2017, Astronomy and Astrophysics, 607, doi: 10.1051/0004-6361/201731335

Van Der Walt, S., Colbert, S. C., & Varoquaux, G. 2011, Computing in Science and Engineering, doi: 10.1109/MCSE.2011.37

van Dokkum, P. 2001, Publications of the Astronomical Society of the Pacific, 113, 1420, doi: 10.1086/323894

van Dokkum, P., Abraham, R., Romanowsky, A. J., et al. 2017, The Astrophysical Journal, 844, L11, doi: 10.3847/2041-8213/aa7ca2

van Dokkum, P., Danieli, S., Cohen, Y., et al. 2018a, Nature, 555, 629, doi: 10.1038/nature25767

van Dokkum, P., Cohen, Y., Danieli, S., et al. 2018b, doi: 10.3847/2041-8213/aab60b

van Dokkum, P. G., Abraham, R., Merritt, A., et al. 2015, The Astrophysical Journal, 798, L45, doi: 10.1088/2041-8205/798/2/L45

Virtanen, P., Gommers, R., Oliphant, T. E., et al. 2020, Nature Methods, 17, 261, doi: 10.1038/s41592-019-0686-2

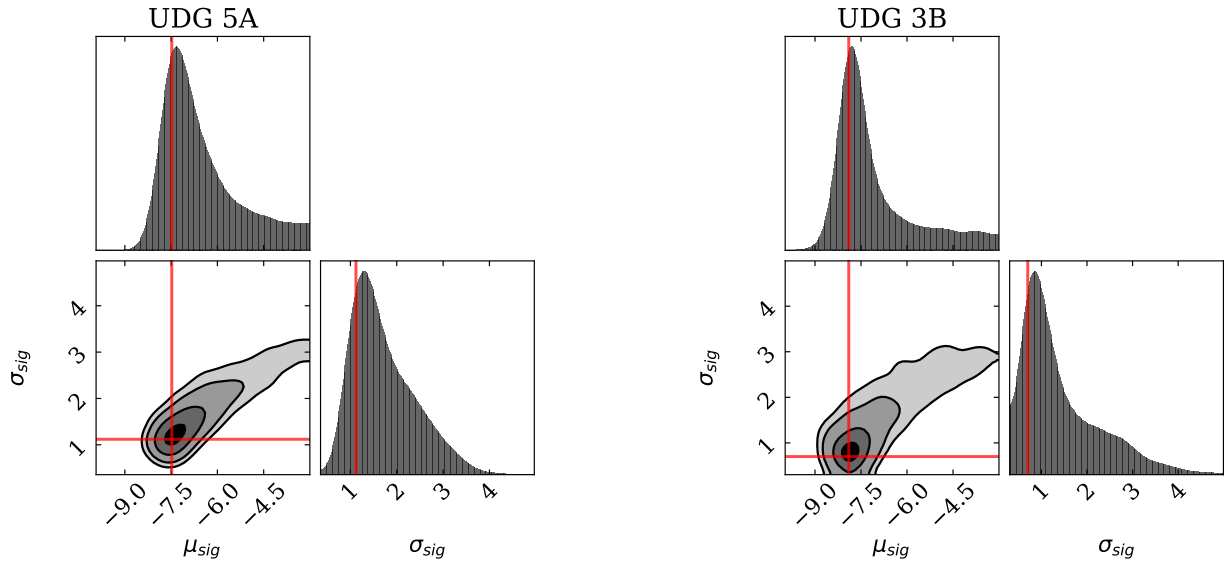
Wechsler, R. H., & Tinker, J. L. 2018, Annual Review of Astronomy and Astrophysics, 56, 435, doi: 10.1146/annurev-astro-081817-051756

Wright, A. C., Tremmel, M., Brooks, A. M., et al. 2020. http://arxiv.org/abs/2005.07634

Yagi, M., Koda, J., Komiyama, Y., & Yamanoi, H. 2016, The Astrophysical Journal Supplement Series, 225, 11, doi: 10.3847/0067-0049/225/1/11

Yang, X., Mo, H. J., van den Bosch, F. C., et al. 2007, The Astrophysical Journal, 671, 153, doi: 10.1086/522027

Yozin, C., & Bekki, K. 2015, Monthly Notices of the Royal Astronomical Society, 452, 937, doi: 10.1093/mnras/stv1073



,

Figure 12. Corner plots showing the correlation between the GCLF mean (μ_{sig}) and width (σ_{sig}) for UDGs 5A (*left*) and 3B (*right*). Red lines mark the best fit GCLF parameters for each UDG. Although these parameters are correlated, the mean and width are clearly peaked for each UDG.

APPENDIX

A. GCLF FITTING PROCEDURE

In this section, we describe our procedure for fitting the UDG globular cluster luminosity functions. We perform a fit directly to the unbinned data using a maximum likelihood formulation. We choose to use an unbinned fit given the low number of GCs, which would not satisfy χ^2 statistics, and the non-negligible photometric errors which would make the choice of bin size complicated in a binned fit. Moreover, our maximum likelihood framework allows us to easily handle the contaminating background population and our incompleteness in a self-contained way. For each UDG we fit the individual, unbinned GC magnitudes to the sum of a signal Gaussian and a background distribution. To account for our completeness, we multiply the signal Gaussian by the completeness functions shown in Figure 5. Thus, for a signal mean and width μ_{sig} and σ_{sig}, a completeness $C(v)$ as a function of V-band magnitude v, and writing a normalized Gaussian as $\mathcal{G}(x \mid \mu, \sigma)$, the probability of observing an actual GC with V-band magnitude v is

$$P_{sig}(v \mid \mu_{sig}, \sigma_{sig}) = \frac{\mathcal{G}(v \mid \mu_{sig}, \sigma_{sig})C(v)}{\int_{-\infty}^{\infty} \mathcal{G}(v' \mid \mu_{sig}, \sigma_{sig})C(v')dv'}.$$

We model the background distribution as a Gaussian, although given the low background level we do not anticipate that variations in this model will affect our results. Given a background mean and width μ_{bkg} and σ_{bkg}, the probability of observing a background source of magnitude v is

$$P_{bkg}(v \mid \mu_{bkg}, \sigma_{bkg}) = \mathcal{G}(v \mid \mu_{bkg}, \sigma_{bkg}).$$

To improve our constraints on the background distribution, we simultaneously fit the galaxy region sources to the combination of the signal and background models and we fit the sources in our background regions to the background distribution. The full model can be summarized by the following log-likelihood, which is a function of the parameters we are most interested in, the signal Gaussian mean and width (μ_{sig} and σ_{sig}), but also the background Gaussian mean and width (μ_{bkg} and σ_{bkg}), the true total number of sources (including background) in the galaxy region (λ_{tot}), and the true number of background sources in the galaxy region (λ_{bkg}). We have written the observed number of sources in the galaxy region as N_{tot}, the observed total number of sources in *all* of the background regions as N_{bkg}, and

the number of background regions as n_{reg} (thus, there is an average of N_{bkg}/n_{reg} background sources per background region, and we expect that the true number of background sources in all of the background regions is $\lambda_{bkg}n_{reg}$). We label galaxy region GCs with the index i and background region GCs by the index j, and denote the corresponding V band magnitudes v_i and v_j.

$$\log \mathcal{L}(\mu_{sig}, \sigma_{sig}, \mu_{bkg}, \sigma_{bkg}, \lambda_{tot}, \lambda_{bkg}) =$$
$$\left\{ -\lambda_{tot} + \sum_{i=1}^{N_{tot}} \log \left[\left(\lambda_{tot} - \frac{\lambda_{bkg}}{n_{reg}} \right) \times P_{sig}(v_i \mid \mu_{sig}, \sigma_{sig}) \right. \right.$$
$$\left. \left. + \left(\frac{\lambda_{bkg}}{n_{reg}} \right) \times P_{bkg}(v_i \mid \mu_{bkg}, \sigma_{bkg}) \right] \right\}$$
$$+$$
$$\left\{ -(n_{reg}\lambda_{bkg}) + \sum_{j=1}^{N_{bkg}} \log \left[(n_{reg}\lambda_{bkg}) P_{bkg}(v_j \mid \mu_{bkg}, \sigma_{bkg}) \right] \right\}.$$

A detailed derivation of the log-likelihood for unbinned data in the Poisson regime can be found in Appendix C of Drlica-Wagner et al. 2020. The first part of this equation is the Poisson log-likelihood for the galaxy region model. The second part contains the Poisson log-likelihood describing the model for the sources in all of the background regions.

We maximize this full log-likelihood to find the best fit μ_{sig} and σ_{sig}, although we do float all parameters, and we evaluate the 1σ errors on these parameters using the `statsmodels` package (Seabold & Perktold 2010). The results are described in Section 4.2 and shown in Figure 7. However, there is a known correlation between the GCLF mean and width (Secker & Harris 1993), which could limit our ability to constrain those parameters. In Figure 12, we show the posterior distributions for the UDG 5A and 3B GCLF means and widths. We evaluated the posterior distribution using the `dynesty` sampler with a stopping criteria $\Delta \log Z = 0.01$. There is a clear correlation between the mean and width for both GCLFs. However, both are strongly peaked, which suggests that our constraints are meaningful.